Graz University of Technology
Institute of Applied Mechanics

Preprint Series

Preprint No 04/2017

Wave propagation in elastic trusses: An approach via retarded potentials

Dominik Pölz, Michael Gfrerer, Martin Schanz
Institute of Applied Mechanics, Graz University of Technology

This is a post-peer-review, pre-copyedit version of the article published in Wave Motion, Volume 87, April 2019, pp 37-57.
The final authenticated version is available online at:
https://doi.org/10.1016/j.wavemoti.2018.06.002

Abstract

We propose a space-time boundary element method for the dynamic simulation of elastic truss systems. The considered truss systems consist of several members, where in each elastic rod the dynamic behaviour is governed by the 1D wave equation. The time domain fundamental solution and boundary integral equations are used to establish the dynamic Dirichlet-to-Neumann map for a single rod. Thus, we are able to reduce the problem to the nodes of the truss system and therefore only a temporal discretization at the truss nodes is necessary. We introduce a stepwise solution strategy with local step size which ensures stability. Furthermore, the discretization within each of these time steps can be refined adaptively to reduce the approximation error efficiently. The optimal convergence of the method is demonstrated in numerical examples. Due to adaptive refinement, this optimal convergence rate is retained even for non-smooth solutions. Finally, the method is applied to study typical truss systems.

1 Introduction

The study of truss and frame structures plays a central role in various fields of engineering. Classical applications in structural engineering include the design of truss bridges and industrial constructions. Recently, the interest in truss and frame structures has been re-sparked by contributions towards modelling nano-structured materials, cf. [24, 20]. The case of elastostatic truss problems is well-understood since direct stiffness methods yield exact solutions. However, the study of elastodynamic truss structures is even today still an open field of research.

There are two fundamentally different approaches to studying the dynamics of mechanical systems: time domain and frequency domain techniques. While frequency domain procedures are well-suited for time harmonic cases, time domain approaches yield fully transient dynamic responses. Most popular methods for time domain simulation employ domain-based approaches for spatial discretization, e.g. finite element methods, in combination with time-stepping schemes to discretize the time variable, cf. [12]. Approximations obtained by representatives of such procedures typically feature oscillations or instabilities when it comes to capturing non-smooth solutions, e.g. due to impact loads. Naturally, various contributions were dedicated towards the development of methods capable of resolving such phenomena more accurately, see e.g. [18, 30, 28]. Other promising techniques for discretizing wave equations, which have not yet been applied to truss systems, are space-time methods. Due to the use of unstructured grids in space and time the approximation can be adapted to local features of the solution in a natural fashion, cf. [19, 7] and the references therein. In contrast to domain-based techniques, boundary integral equation (BIE) methods reduce the problem to the boundary, which is given by the nodes in the case of truss systems. Thus, the discretization of these BIEs by means of boundary element methods (BEM) does not need to introduce any spatial discretization. Although the BIE method has already been successfully applied to studying elastodynamic truss and frame structures, literature is scarce compared to more conventional approaches, see e.g. [8, 11]. In [8], frequency domain fundamental solutions are employed and time domain solutions are recovered via convolution quadrature. In [11], the fundamental solution of the related static differential equation is used and the inertia term is not shifted to the boundary by means of integral equations but remains as domain integral. In contrast to these techniques, we seek an approach based on time domain BIEs, using the fundamental solution of the hyperbolic equation.

The mathematical aspects of time domain BIEs for the wave equation have first been studied extensively in the pioneering work of Bamberger and Ha-Duong [9, 10], see [13] for an exhaustive review. In more recent contributions Aimi and her collaborators introduced the so-called *energetic Galerkin BEM* [2, 4, 6]. Their developed bilinear forms are closely related to those analysed by Bamberger and Ha-Duong. The only difference is that the energetic bilinear forms omit the prominent weighting function $t \mapsto e^{-2\sigma t}$ for some $\sigma > 0$. As stated in [16, 27] the estimates of the bilinear forms obtained by the Bamberger and Ha-Duong method do not pass to the limit $\sigma \to 0$. In contrast, numerical experiments indicate that stable approximations can be achieved even for $\sigma = 0$, see e.g. [17]. The time domain analysis in [2] shows that this weight can indeed be dropped for the 1D wave equation, while retaining ellipticity of the standard bilinear forms.

This work is dedicated towards applying the energetic BIE method to study elastodynamic

truss systems. The proposed formulation is directly related to direct stiffness methods known for elastostatic systems. The novelty of our approach lies in the application to dynamic problems. A great advantage of the proposed space-time BIE method over existing BIE formulations is that it handles non-smooth solutions remarkably well. On the one hand the space-time variational formulations have rather low regularity assumptions about the right hand side, admitting discontinuous functions. On the other hand non-uniform discretizations enable the accurate resolution of solutions with low regularity. As shown in Section 5, this advantage is even more compelling when adaptive mesh refinement strategies are employed.

A truss structure is an assembly of bar members connected by hinges. In a static setting no bending moments and transversal forces occur, if loads are applied only at the hinges. Thus only longitudinal forces have to be considered. In the dynamic case, bending moments and transversal forces occur due to inertia effects. However, in the present paper the physical model is based on the following assumptions:

- Interior forces orthogonal to the axes of the bar members as well as bending moments are neglected.
- Inertia terms induced by accelerations orthogonal to the axes of the bar members and rotation of the bar members are omitted.
- The material is assumed to have no damping.

A justification or limitation of the applicability of the physical model is beyond the scope of the present paper. However, under these assumptions, we can describe the dynamics of the truss system by clear-cut time domain BIEs. As discussed in Section 5, the results of this approach are satisfactory and an extension to models that are physically complete is worth striving for.

The outline of this paper is as follows. In Section 2, a single rod problem is reformulated in terms of time domain BIEs. This concept is extended to truss structures by means of appropriate kinematic and kinetic coupling conditions connecting the individual rods in Section 3. The discretization of the variational formulation is addressed in Section 4. Finally, numerical examples are presented in Section 5 confirming the implementation and performance of the discussed procedures.

2 BIEs for elastodynamic rods

We consider an elastic rod (also referred to as member) with length $L > 0$, Young's modulus $E > 0$, cross-sectional area $A > 0$, and mass density $\rho > 0$. The wave speed is given by $c = \sqrt{E/\rho}$. Moreover, let $T > 0$ be some fixed simulation end time. The space-time cylinder of this member is the rectangle $Q := (0,L) \times (0,T)$ and its lateral boundary is denoted $\Sigma := \{0,L\} \times (0,T)$. We are concerned with finding longitudinal displacement functions of the member $u_m : Q \to \mathbb{R}$ satisfying the homogeneous 1D elastodynamic wave equation

$$c^{-2}\ddot{u}_m(x,t) - \partial_x^2 u_m(x,t) = 0, \quad (x,t) \in Q \tag{1}$$

and the homogeneous initial conditions

$$u_m(x,0) = \dot{u}_m(x,0) = 0, \quad x \in (0,L) \tag{2}$$

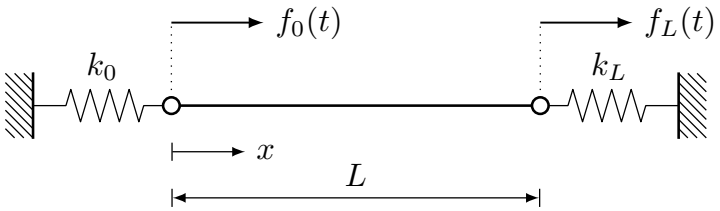

Figure 1: The mechanical system modelled by the Robin initial boundary value problem (1)–(3).

where dots over functions denote derivatives with respect to the time variable, and ∂_x denotes the spatial derivative. The inner force function of the member is defined $p_m(x,t) \coloneqq EA\,\partial_x u_m(x,t)$ for $(x,t) \in Q$.

Within a BIE approach, we are especially interested in the Cauchy data of the solution. To this extent, we define vector-valued functions for the Dirichlet data $u(t) \coloneqq [u_0(t), u_L(t)]^\top$ and the Neumann data $p(t) \coloneqq [-p_0(t), p_L(t)]^\top$. The subscript indicates the spatial coordinate, e.g. $u_0(t) \coloneqq u_m(0,t)$ and $u_L(t) \coloneqq u_m(L,t)$ for $t \in (0,T)$. A useful model problem, which serves as preparation for the truss system, is posed by the Robin boundary condition

$$p(t) + K_s u(t) = f(t), \quad t \in (0,T). \tag{3}$$

Hereby, $K_s = [k_0, 0; 0, k_L]$ is a stiffness matrix with spring stiffnesses $k_0, k_L \geq 0$ and $f(t) = [f_0(t), f_L(t)]^\top$ is the external loading function. An illustration of the mechanical system modelled by (1)–(3) is provided in Figure 1. Throughout this work, we assume that all functions in time are defined on the entire real line, however, they are supported only on the provided interval, i.e. $[0,T]$. In particular, this implies causality of all considered functions.

The following outline of time domain BIEs for the 1D wave equation is based on [2, 4]. In contrast to these works which focus on Dirichlet and Neumann boundary value problems, our focus lies on the Robin boundary condition (3). For sufficiently smooth densities $w, v : \Sigma \to \mathbb{R}$ the single layer potential

$$\mathrm{SL}[w](x,t) \coloneqq \frac{c}{2EA} \int_0^{t-\frac{x}{c}} w_0(s)\,\mathrm{d}s + \frac{c}{2EA} \int_0^{t+\frac{x-L}{c}} w_L(s)\,\mathrm{d}s, \quad (x,t) \in Q$$

and the double layer potential

$$\mathrm{DL}[v](x,t) \coloneqq -\frac{1}{2} v_0\left(t - \frac{x}{c}\right) - \frac{1}{2} v_L\left(t + \frac{x-L}{c}\right), \quad (x,t) \in Q$$

define solutions of (1) and (2). These are *retarded potentials*, since the space-time coordinate (x,t) occurs as shifted argument $t \pm \frac{x}{c}$. The single layer potential integrates over the part of the lateral boundary that is lit by the backward light cone of (x,t), whereas the double layer potential evaluates at the points of the lateral boundary that lie on that cone. Using these potentials the usual representation formula holds

$$u_m(x,t) = \mathrm{SL}[p](x,t) - \mathrm{DL}[u](x,t), \quad (x,t) \in Q \tag{4}$$

for any solution of (1) and (2). Since we are interested in solutions of the initial boundary value problem, functions p and u have to be determined such that (3) holds. To compute the unknown Cauchy data, the limits $x \to 0$ and $x \to L$ are performed in (4), yielding the set of BIEs

$$\frac{c}{EA}\int_0^t p_0(s)\,\mathrm{d}s + \frac{c}{EA}\int_0^{t-\frac{L}{c}} p_L(s)\,\mathrm{d}s = u_0(t) - u_L\left(t-\frac{L}{c}\right)$$
$$\frac{c}{EA}\int_0^{t-\frac{L}{c}} p_0(s)\,\mathrm{d}s + \frac{c}{EA}\int_0^{t} p_L(s)\,\mathrm{d}s = -u_0\left(t-\frac{L}{c}\right) + u_L(t)$$

for $t \in (0,T)$. For our purposes it is convenient to consider the time derivative of these BIEs, leading to

$$\frac{c}{EA}\left(\mathrm{A}\,p\right)(t) = \left(\mathrm{B}\,\dot{u}\right)(t), \quad t \in (0,T) \tag{5}$$

with the operator matrices

$$\mathrm{A} := \begin{bmatrix} \mathrm{I} & \mathrm{S} \\ \mathrm{S} & \mathrm{I} \end{bmatrix}, \quad \mathrm{B} := \begin{bmatrix} \mathrm{I} & -\mathrm{S} \\ -\mathrm{S} & \mathrm{I} \end{bmatrix}$$

and the retarded shift operator S defined by its action on a suitable $g : (0,T) \to \mathbb{R}$

$$\left(\mathrm{S}\,g\right)(t) := \theta\left(t-\frac{L}{c}\right) g\left(t-\frac{L}{c}\right), \quad t \in (0,T) \tag{6}$$

where $\theta(t)$ denotes the Heaviside step function. We note that $\mathrm{S} : L^2(0,T) \to L^2(0,T)$ as well as $\mathrm{S} : H^1_{\{0\}}(0,T) \to H^1_{\{0\}}(0,T)$ are bounded, where $H^1_{\{0\}}(0,T)$ denotes the space of H^1-functions vanishing at $t = 0$. The functional framework outlined in [2, 4] considers Neumann data p belonging to the space $L^2(\Sigma) := L^2(0,T) \times L^2(0,T)$ and Dirichlet data u in $H^1_{\{0\}}(\Sigma) := H^1_{\{0\}}(0,T) \times H^1_{\{0\}}(0,T)$. In this setting, the representation formula (4) defines distributional solutions of (1) and (2) in a subspace of $H^1(Q)$ for any $p \in L^2(\Sigma)$ and $u \in H^1_{\{0\}}(\Sigma)$.

As shown in [4], the operators $\mathrm{A}, \mathrm{B} : L^2(\Sigma) \to L^2(\Sigma)$ are isomorphisms. Hence, for each $u \in H^1_{\{0\}}(\Sigma)$ there exists a unique $p \in L^2(\Sigma)$ that solves (5). As an immediate consequence, the Dirichlet-to-Neumann map $\mathrm{DtN} : H^1_{\{0\}}(\Sigma) \to L^2(\Sigma)$

$$p = \mathrm{DtN}\,u = \frac{EA}{c}\,\mathrm{A}^{-1}\,\mathrm{B}\,\dot{u} \tag{7}$$

is well-defined. For convenience, we define the operator $\mathrm{C} := \mathrm{A}^{-1}\,\mathrm{B}$ where $\mathrm{C} : L^2(\Sigma) \to L^2(\Sigma)$ is bounded and write $\mathrm{DtN}\,u = \frac{EA}{c}\,\mathrm{C}\,\dot{u}$ for $u \in H^1_{\{0\}}(\Sigma)$. Via (7) the Dirichlet data of a given solution of (1) and (2) are mapped onto the corresponding Neumann data. In other words, the axial forces at the end points of the rod can be computed using only the displacement functions at these points via this map.

To realize the Dirichlet-to-Neumann map within a computer simulation efficiently, an explicit and computable representation of (7) is desirable. For the problem at hand, such an explicit

representation can indeed be derived. We start by noting hat the inverse of the operator $\mathrm{A} : L^2(\Sigma) \to L^2(\Sigma)$ is given by

$$\mathrm{A}^{-1} = \begin{bmatrix} \left(\mathrm{I}-\mathrm{S}^2\right)^{-1} & -\mathrm{S}\left(\mathrm{I}-\mathrm{S}^2\right)^{-1} \\ -\mathrm{S}\left(\mathrm{I}-\mathrm{S}^2\right)^{-1} & \left(\mathrm{I}-\mathrm{S}^2\right)^{-1} \end{bmatrix} \tag{8}$$

if the inverse of $\mathrm{I}-\mathrm{S}^2$ exists. The inverse exists and has the representation

$$\left(\mathrm{I}-\mathrm{S}^2\right)^{-1} = \sum_{j=0}^{\infty} \mathrm{S}^{2j}$$

if the Neumann series converges. From (6) it can be concluded that $\mathrm{S} : L^2(0,T) \to L^2(0,T)$ is a nilpotent operator, in particular the iterated operator S^j is zero for $j \geq \left\lceil \frac{Tc}{L} \right\rceil$. For convenience of notation, define the number of nonzero double shifts $n := \left\lceil \frac{Tc}{2L} \right\rceil$. Due to the nilpotency of the shift operator the Neumann series coincides with its n-th partial sum for which the bound

$$\left\| \sum_{j=0}^{n-1} \mathrm{S}^{2j} \right\| \leq \sum_{j=0}^{n-1} \left\| \mathrm{S}^{2j} \right\| \leq \sum_{j=0}^{n-1} \|\mathrm{S}\|^{2j} \leq n$$

holds by the triangle inequality and $\|\mathrm{S}\| \leq 1$. It follows that the inverse of $\mathrm{I}-\mathrm{S}^2$ exists and has the representation

$$\left(\mathrm{I}-\mathrm{S}^2\right)^{-1} = \sum_{j=0}^{n-1} \mathrm{S}^{2j}. \tag{9}$$

Insertion of (9) in (8) and (7) yields the explicit representation of the map $\mathrm{DtN} : u \mapsto \frac{EA}{c}\,\mathrm{C}\,\dot{u}$ with the operator matrix

$$\mathrm{C} := 2\sum_{j=0}^{n-1} \begin{bmatrix} \mathrm{S}^{2j} & -\mathrm{S}^{2j+1} \\ -\mathrm{S}^{2j+1} & \mathrm{S}^{2j} \end{bmatrix} - \mathrm{I}. \tag{10}$$

Remark 1. Instead of solving (5) for the Neumann data, it could also be solved for the Dirichlet data. In particular, for each $p \in L^2(\Sigma)$, there exists a unique $\dot{u} \in L^2(\Sigma)$ that solves (5). By integration, a unique $u \in H^1_{\{0\}}(\Sigma)$ that solves (5) and vanishes at $t = 0$ is obtained. This gives rise to the Neumann-to-Dirichlet map $\mathrm{NtD} : L^2(\Sigma) \to H^1_{\{0\}}(\Sigma)$

$$u = \mathrm{NtD}\,p = \frac{c}{EA}\partial_t^{-1}\,\mathrm{B}^{-1}\,\mathrm{A}\,p$$

where the primitive $\partial_t^{-1} : L^2(0,T) \to H^1_{\{0\}}(0,T)$ is defined by

$$\left(\partial_t^{-1} g\right)(t) := \int_0^t g(s)\,\mathrm{d}s$$

and applied element-wise. Inspection of the involved operators confirms that $\mathrm{DtN}^{-1} = \mathrm{NtD}$ holds. Furthermore, we find the explicit representation $\mathrm{NtD} : p \mapsto \frac{c}{EA}\,\mathrm{D}\,\partial_t^{-1} p$ where $\mathrm{D} = \mathrm{C}^{-1}$ differs from C in (10) only in the sign of the off-diagonal terms. To derive this expression, we used that the operators ∂_t^{-1} and S commute, consequently ∂_t^{-1} and D commute as well. Since this work focuses on displacement-based formulations, the Neumann-to-Dirichlet map is not considered any further.

2.1 Energetic one-shot solution of single rod problems

Using (7) the Robin boundary condition (3) can be reformulated in terms of the Dirichlet data only

$$(\mathrm{DtN}\, u)(t) + K_s u(t) = f(t), \quad t \in (0,T). \tag{11}$$

To find a viable variational formulation of (11), we use the same energy argument as in [2]. The energy within the rod is defined by

$$\mathcal{E}(u_m,t) \coloneqq \frac{EA}{2}\int_0^L \left[\left(c^{-1}\dot{u}_m(x,t)\right)^2 + \left(\partial_x u_m(x,t)\right)^2\right] \mathrm{d}x \geq 0,$$

which is the sum of kinetic and strain energy. Sufficiently smooth solutions u_m of the wave equation satisfy the energy-flux relation

$$0 = \dot{u}_m\left(c^{-2}\ddot{u}_m - \partial_x^2 u_m\right) = \partial_t\left(\frac{1}{2}c^{-2}\dot{u}_m^2 + \frac{1}{2}\left(\partial_x u_m\right)^2\right) - \partial_x\left(\dot{u}_m \partial_x u_m\right)$$

which is integrated over Q yielding the energy identity at final time

$$\mathcal{E}(u_m,T) = \int_0^T \left[p_m(L,t)\,\dot{u}_m(L,t) - p_m(0,t)\,\dot{u}_m(0,t)\right] \mathrm{d}t = \int_0^T p(t)\cdot\dot{u}(t)\,\mathrm{d}t, \tag{12}$$

since the energy at $t=0$ vanishes due to (2). From these considerations, we infer that an appropriate formulation might be achieved by projecting (11) onto time derivatives of admissible displacements. The variational problem reads:
Given $f \in L^2(\Sigma)$, find $u \in H^1_{\{0\}}(\Sigma)$ such that

$$(\mathrm{DtN}\, u, \dot{v})_{L^2(\Sigma)} + (K_s u, \dot{v})_{L^2(\Sigma)} = (f, \dot{v})_{L^2(\Sigma)} \tag{13}$$

holds for all $v \in H^1_{\{0\}}(\Sigma)$. Despite of property (12), the bilinear form $a : H^1_{\{0\}}(\Sigma) \times H^1_{\{0\}}(\Sigma) \to \mathbb{R}$ defined by

$$a(u,v) \coloneqq (\mathrm{DtN}\, u, \dot{v})_{L^2(\Sigma)} = \frac{EA}{c}(\mathrm{C}\,\dot{u}, \dot{v})_{L^2(\Sigma)} \tag{14}$$

is not elliptic for $Tc > L$. In particular there exists a non-trivial $v \in H^1_{\{0\}}(\Sigma)$ such that $a(v,v) = 0$. An example for such a function is given by

$$\begin{aligned}
&\dot{v}(t) = \left[\varphi(t), \varphi(t)\right]^\top, \\
&\varphi(t) = \theta(t) - \theta\left(t + \tfrac{L}{c} - T\right) + \theta\left(t - \tfrac{L}{c}\right) && \text{for } L < Tc \leq 2L, \\
&\varphi(t) = \theta\left(t + \tfrac{2L}{c} - T\right) && \text{for } 2L < Tc.
\end{aligned}$$

However, the energetic bilinear form is elliptic for $Tc \leq L$, since $\mathrm{C} = \mathrm{I}$ in this case. Thus, existence and uniqueness of a solution for any $f \in L^2(\Sigma)$ is guaranteed by the Lax-Milgram lemma. A similar result in a more general setting has already been shown in [1]. By solving (13) one obtains the solution in the entire time interval $[0,T]$ at once. That is why we call this type of solution strategy "one-shot" solution, see also [2, Rem. 3]. However, one could

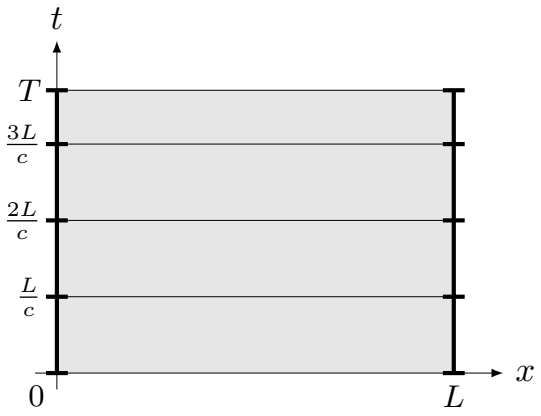

Figure 2: Decomposition of Σ into four space-time slabs of length at most $\frac{L}{c}$.

also decompose $[0,T]$ into subintervals, such that a set of smaller problems instead of one large problem has to be solved. By causality these subproblems can be solved in sequence, which is why this approach is called "stepwise" solution. This strategy is explored in the following subsection.

2.2 Stepwise solution of single rod problems

In addition to solving in one shot for the entire space-time boundary, we provide an approach that decomposes (13) into a set of variational problems posed on subintervals of $[0,T]$. The idea of this procedure is based on the finite speed of propagation of the underlying hyperbolic equation, i.e. signals emitted at time t from one end of the rod are perceived at the other end at $t+\frac{L}{c}$. Hence, the lateral boundary Σ is decomposed into a fixed number of so-called space-time slabs. The number of slabs is defined $n_s := \lceil \frac{Tc}{L} \rceil$ and the slabs are given by

$$\Sigma_j := \begin{cases} \{0,L\} \times \left((j-1)\frac{L}{c}, j\frac{L}{c}\right] & j = 1,\dots,n_s-1, \\ \{0,L\} \times \left((j-1)\frac{L}{c}, T\right) & j = n_s. \end{cases}$$

Such a decomposition of Σ into space-time slabs is illustrated in Figure 2. To keep notation simple, for $j = 1,\dots,n_s$ the function $\widetilde{u}_j : \Sigma \to \mathbb{R}$ is defined as extension of a function on the slab $u_j : \Sigma_j \to \mathbb{R}$ to the entire space-time boundary

$$\widetilde{u}_j(x,t) := \begin{cases} u_j(x,t) & (x,t) \in \Sigma_j, \\ u_j\left(x, j\frac{L}{c}\right) & (x,t) \in \{0,L\} \times \left(j\frac{L}{c}, T\right), \\ 0 & (x,t) \in \{0,L\} \times \left(0, (j-1)\frac{L}{c}\right], \end{cases} \tag{15}$$

i.e. the function is extended trivially to the past and continuously constant to the future. Assume now that the solutions u_ℓ for $\ell = 1,\dots,j-1$ have already been computed, and we wish to find the solution at the currently observed slab j. To this extent, the solution up to slab j is split

into the extensions of an unknown solution on the current slab and the known solutions on the previous slabs

$$u(x,t) = \widetilde{u}_j(x,t) + \sum_{\ell=1}^{j-1} \widetilde{u}_\ell(x,t), \quad (x,t) \in \bigcup_{\ell=1}^{j} \Sigma_\ell \,. \tag{16}$$

Note that due to (15) expression (16) defines a function in $H^1_{\{0\}}(\Sigma)$ when $u_\ell \in H^1_{\{0\}}(\Sigma_\ell)$ holds for all $\ell = 1,\dots,j$. By plugging (16) into (13) while considering the L^2 scalar product only on Σ_j a modified formulation is obtained at the space-time slab. The action of the Dirichlet-to-Neumann map on the unknown part reduces to $\mathrm{DtN}\widetilde{u}_j = \frac{EA}{c}\dot{u}_j$ in Σ_j. The variational problem at the j-th slab reads:
Given $f \in L^2(\Sigma)$ and $(\widetilde{u}_\ell)_{\ell=1,\dots,j-1}$, find $u_j \in H^1_{\{0\}}(\Sigma_j)$ such that

$$b_j(u_j, v_j) = (f, \dot{v}_j)_{L^2(\Sigma_j)} - \sum_{\ell=1}^{j-1} (K_s \widetilde{u}_\ell, \dot{v}_j)_{L^2(\Sigma_j)} - \sum_{\ell=1}^{j-1} (\mathrm{DtN}\,\widetilde{u}_\ell, \dot{v}_j)_{L^2(\Sigma_j)} \tag{17}$$

holds for all $v_j \in H^1_{\{0\}}(\Sigma_j)$. The bilinear form $b_j : H^1_{\{0\}}(\Sigma_j) \times H^1_{\{0\}}(\Sigma_j) \to \mathbb{R}$ is defined by

$$b_j(u_j, v_j) \coloneqq \frac{EA}{c} (\dot{u}_j, \dot{v}_j)_{L^2(\Sigma_j)} + (K_s u_j, \dot{v}_j)_{L^2(\Sigma_j)} \,. \tag{18}$$

After solving (17) sequentially for $j = 1,\dots,n_s$ the desired solution $u : \Sigma \to \mathbb{R}$ is given by (16) with $j = n_s$. The bilinear form (18) is elliptic, ensuring unique solvability of the problem for each $j = 1,\dots,n_s$. Moreover, the solution is stable, i.e. it depends continuously on the given data. However, the solution on slab j depends on the solution of all previous slabs, and thus the stability constant occurring in the Lax-Milgram lemma grows significantly with n_s. We emphasize that solving (17) sequentially for all $j = 1,\dots,n_s$ and inserting the solutions into (16) is equivalent to solving (13). Note that within an implementation it is sufficient to store only the sum in (16) instead of keeping track of all summands individually.

We emphasise that the idea of solving hyperbolic partial differential equations in space-time by such a stepwise approach is not new. Our sequential approach, and its inherent constraint on the size of the space-time slabs, is quite similar to more general finite element methods proposed in the early contributions [26, 21]. The interested reader is also referred to the recent work [15] and the references therein for an overview of these procedures, especially in the context of space-time discontinuous Galerkin methods.

3 BIEs for elastodynamic truss structures

A truss is a mechanical assembly of rod elements (members), forming a structure in d-dimensional space, where $d = 2,3$. The individual members are connected to each other via hinges at their end points. Thus, the relative rotation of the rods connected by a hinge is not constrained. At least d of these nodes are supported, restraining their movement. Each unsupported node has to have at least d members linked to it, which is necessary to prevent the occurrence of kinematic chains in the structure. External loads are applied only at the nodes of the structure. Moreover, we assume that there are no lumped masses at the joints. All displacements considered

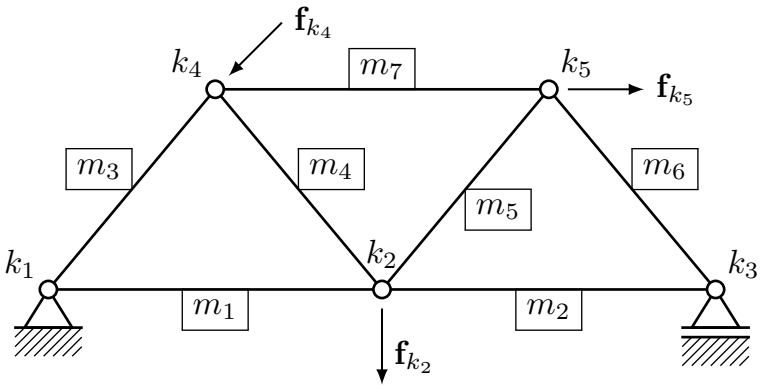

Figure 3: Sketch of a typical truss structure. In this case $\mathcal{T} = \{m_1, \ldots, m_7\}$ and $\mathcal{N}_\mathcal{T} = \{k_1, \ldots, k_5\}$. Nonzero external forces are applied to nodes k_2, k_4, and k_5. Examples of the defined sets are given by $\mathcal{N}_\mathcal{S} = \{k_1, k_3\}$, $\beta_{k_2} = \{m_1, m_2, m_4, m_5\}$, and $\kappa_{m_6} = \{k_3, k_5\}$.

in this section are interpreted as (sufficiently small) displacements relative to a static state of equilibrium that is due to the self-weight of the members.

Since the nodes may perform arbitrary (but sufficiently small) motions in d-dimensional space, lateral accelerations of the connected members are going to be of the same magnitude as the longitudinal ones. Due to these accelerations, transversal forces and bending moments are necessary in order to satisfy dynamic equilibrium at each point in each member. As already mentioned in the introduction, these effects are neglected. It is assumed that truss members only transmit axial forces, but neither transversal forces nor bending moments. Moreover, lateral and rotational inertia effects are neglected. To stay in line with Section 2, we assume that there is no material damping. From a mechanical point of view, this poses a severe restriction of the model, however, enables a thorough study of the performance of time domain BIEs for this simplified model. We shall comment on the incorporation of these effects at the end of this section.

To come up with a systematic description of the truss system, we denote the set of truss members $\mathcal{T}$ and the set of truss nodes $\mathcal{N}_\mathcal{T}$. The set of supported nodes is denoted $\mathcal{N}_\mathcal{S} \subsetneq \mathcal{N}_\mathcal{T}$. The set of free nodes is the relative complement $\mathcal{N}_\mathcal{F} = \mathcal{N}_\mathcal{T} \setminus \mathcal{N}_\mathcal{S}$. Each node $k \in \mathcal{N}_\mathcal{T}$ has a set of attached truss members $\beta_k \subset \mathcal{T}$. Moreover, every member $m \in \mathcal{T}$ has precisely two nodes connected to it, collected in the set $\{k_{m0}, k_{mL}\} =: \kappa_m \subset \mathcal{N}_\mathcal{T}$. An illustration of a typical truss structure is provided in Figure 3. We denote by $\mathbf{r}_m$ the unit tangential vector and $\mathbf{n}_m^\ell$ for $\ell = 1, \ldots, d-1$ the unit normal vectors of each member m. Note that the vector $\mathbf{r}_m$ is defined to point from k_{m0} to k_{mL}. Furthermore, each member m is associated with individual parameters L_m, E_m, A_m, and c_m as defined in Section 2. For convenience of notation we introduce the $\mathbb{R}^{d\times d}$ matrices

$$M_m := \frac{E_m A_m}{c_m} \mathbf{r}_m \otimes \mathbf{r}_m \quad , \quad J_k := \sum_{m \in \beta_k} M_m$$

which can be interpreted as instantaneous stiffness matrices of member $m \in \mathcal{T}$ and node $k \in \mathcal{N}_\mathcal{T}$

respectively. Throughout this work, we assume that $J_k : \mathbb{R}^d \to \mathbb{R}^d$ is surjective for every $k \in \mathcal{N}_F$. This assumption will guarantee that there exists a solution, i.e. a state of equilibrium, to the problems discussed in this section. The determinant of the matrix J_k is nonzero if and only if there are d linearly independent vectors $\mathbf{r}_m$ for $m \in \beta_k$. In this case the symmetric matrix J_k is positive definite. For $d = 2$ this condition implies that the tangential vectors of at least two members in β_k are not collinear. In the case $d = 3$ it is equivalent to the tangential vectors of all members in β_k not lying on the same plane. These criteria for the topology of the truss system are well-known from the static case and apply to our dynamic model as well due to the limitation to axial interior forces only.

The space-time skeleton of the truss is defined $\Sigma_{\mathcal{T}} \coloneqq \mathcal{N}_{\mathcal{T}} \times (0,T)$. The displacement function on the skeleton $\mathbf{u} : \Sigma_{\mathcal{T}} \to \mathbb{R}^d$ describes the movement of all nodes of the truss. By restriction, a nodal displacement function $\mathbf{u}|_k : (0,T) \to \mathbb{R}^d$ is obtained for each $k \in \mathcal{N}_{\mathcal{T}}$. Due to the motion of the nodes, the connected bars are deformed. Thus, each member $m \in \mathcal{T}$ has an associated displacement function $\mathbf{u}_m : Q_m \to \mathbb{R}^d$, where $Q_m \coloneqq (0,L_m) \times (0,T)$. It is suitable to decompose the vector-valued displacement function $\mathbf{u}_m$ into a longitudinal displacement function $u_m : Q_m \to \mathbb{R}$ and transversal displacement functions $w_{m,\ell} : Q_m \to \mathbb{R}$, where $\ell = 1, \dots, d-1$. Thus, the displacement function is represented by its components via

$$\mathbf{u}_m(x,t) = u_m(x,t)\,\mathbf{r}_m + \sum_{\ell=1}^{d-1} w_{m,\ell}(x,t)\,\mathbf{n}_m^\ell, \quad (x,t) \in Q_m. \tag{19}$$

Since we assume linear elastic material behaviour and small deformations, the axial displacement function u_m is governed by (1) and (2) for every $m \in \mathcal{T}$. Therefore, the function u_m can be represented by means of (4). Note that the transversal displacement functions $w_{m,\ell}$ for $\ell = 1, \dots, d-1$ can be obtained by projecting $\mathbf{u}|_k$ onto $\mathbf{n}_m^\ell$ for each $k \in \kappa_m$ and linear interpolation of these nodal displacement values along the rod. This is justified by the fact, that due to the absence of bending moments, the curvature of each rod has to vanish. In the setting of small deformations this is achieved only by displacement functions linear in the spatial variable.

Moreover, each truss member is equipped with an inner force function $\mathbf{p}_m : Q_m \to \mathbb{R}^d$. Due to the simplification of the mechanical model to account for axial forces only, this function reduces to $\mathbf{p}_m(x,t) = p_m(x,t)\,\mathbf{r}_m$ where $p_m(x,t) = E_m A_m\, \partial_x u_m(x,t)$ for $(x,t) \in Q_m$ is the longitudinal force component. To keep the exposition as close to Section 2 as possible, we define the traces of this force function by

$$\mathbf{p}_m|_k(t) \coloneqq \begin{cases} -p_m(0,t)\,\mathbf{r}_m & k = k_{m0} \\ p_m(L_m,t)\,\mathbf{r}_m & k = k_{mL} \end{cases}, \quad t \in (0,T). \tag{20}$$

To avoid the occurrence of gaps in between the node k and the connected members β_k, the displacement function of every member $m \in \mathcal{T}$ has to satisfy the kinematic compatibility condition

$$\mathbf{u}_m|_k(t) = \mathbf{u}|_k(t), \quad t \in (0,T) \tag{21}$$

for each $k \in \kappa_m$. Here $\mathbf{u}_m|_k$ denotes the trace of the function $\mathbf{u}_m : Q_m \to \mathbb{R}^d$ to the end point at node k. Additionally, the nodal equilibrium

$$-\sum_{m \in \beta_k} \mathbf{p}_m|_k(t) + \mathbf{f}_k(t) = \mathbf{0}, \quad t \in (0,T) \tag{22}$$

has to hold for every $k \in \mathcal{N}_F$, where $\mathbf{f}_k : (0,T) \to \mathbb{R}^d$ is the external nodal load. Note that the negative sign in (22) is due to definition (20). The axial force component $p_m : Q_m \to \mathbb{R}$ can be represented by a properly defined Dirichlet-to-Neumann map, which takes the parameters of member m into account. Hence, we define the number of shifts $n_m := \left\lceil \frac{T c_m}{2L_m} \right\rceil$ and the operator S_m as in (6) but with parameters L_m and c_m for every member $m \in \mathcal{T}$. Consequently, we obtain the explicit representation of the Dirichlet-to-Neumann map

$$\mathrm{DtN}_m : u \mapsto \frac{E_m A_m}{c_m} \mathrm{C}_m \dot{u} \quad \text{with} \quad \mathrm{C}_m := 2 \sum_{j=0}^{n_m - 1} \begin{bmatrix} \mathrm{S}_m^{2j} & -\mathrm{S}_m^{2j+1} \\ -\mathrm{S}_m^{2j+1} & \mathrm{S}_m^{2j} \end{bmatrix} - \mathrm{I} \tag{23}$$

for each member $m \in \mathcal{T}$. As a result, the nodal equilibrium condition can be rewritten in terms of displacements

$$-\sum_{m \in \beta_k} \left([\mathrm{DtN}_m u_m|_{\kappa_m}]|_k \, \mathbf{r}_m \right)(t) + \mathbf{f}_k(t) = \mathbf{0}, \quad t \in (0,T)$$

for each $k \in \mathcal{N}_F$. Utilizing (21) and decomposition (19) we can define the nodal force operator P_k by its action

$$\mathrm{P}_k : \mathbf{u} \mapsto \sum_{m \in \beta_k} [\mathrm{DtN}_m (\mathbf{u}|_{\kappa_m} \cdot \mathbf{r}_m)]|_k \, \mathbf{r}_m. \tag{24}$$

The dot product in (24) is, in a slight abuse of notation, defined by

$$\mathbf{u}|_{\kappa_m} \cdot \mathbf{r}_m := [\mathbf{u}|_{k_{m0}} \cdot \mathbf{r}_m, \mathbf{u}|_{k_{mL}} \cdot \mathbf{r}_m]^\top.$$

The operator (24) acts in the following way: it restricts the displacement function on the skeleton to longitudinal displacement at the end points of an attached member, applies its Dirichlet-to-Neumann map to compute axial forces, and sets up the nodal force vector via restriction. By summing over all connected rods, the resulting force function at node k is obtained. Hence, the truss problem in strong form boils down to finding $\mathbf{u} : \Sigma_{\mathcal{T}} \to \mathbb{R}^d$ which vanishes at $t = 0$ and $\mathbf{u}|_k = \mathbf{0}$ for all $k \in \mathcal{N}_S$ such that

$$(\mathrm{P}_k \mathbf{u})(t) = \mathbf{f}_k(t), \quad t \in (0,T) \tag{25}$$

holds for each $k \in \mathcal{N}_F$.

3.1 Energetic one-shot solution of truss problems

To obtain a variational formulation similar to (13), we want to project (25) onto time derivatives of suitable test functions. To do so, the energy space of the truss is defined

$$\mathbf{H}_{\mathcal{T}} := \left\{ \mathbf{v} \in \bigtimes_{k \in \mathcal{N}_{\mathcal{T}}} \mathbf{H}^1_{\{0\}}(0,T) : \mathbf{v}|_k = \mathbf{0}, k \in \mathcal{N}_S \right\}. \tag{26}$$

Note that the nodal force operator $\mathrm{P}_k : \mathbf{H}_{\mathcal{T}} \to \mathbf{L}^2(0,T)$ is bounded for all $k \in \mathcal{N}_{\mathcal{T}}$. A variational formulation of (25) is obtained by performing the Euclidean scalar product with the nodal restriction $\dot{\mathbf{v}}|_k$ of a displacement test function $\mathbf{v} \in \mathbf{H}_{\mathcal{T}}$, integration in time, and summation over all

nodes $k \in \mathcal{N}_F$. The variational problem reads:
Given nodal forces $\mathbf{f}_k \in \mathbf{L}^2(0,T)$ for $k \in \mathcal{N}_F$, find $\mathbf{u} \in \mathbf{H}_\mathcal{T}$ such that

$$a_\mathcal{T}(\mathbf{u},\mathbf{v}) = f_\mathcal{T}(\mathbf{v}) \tag{27}$$

holds for all $\mathbf{v} \in \mathbf{H}_\mathcal{T}$ with the bilinear form $a_\mathcal{T} : \mathbf{H}_\mathcal{T} \times \mathbf{H}_\mathcal{T} \to \mathbb{R}$

$$a_\mathcal{T}(\mathbf{u},\mathbf{v}) \coloneqq \sum_{k\in\mathcal{N}_F} (\mathrm{P}_k \mathbf{u}, \dot{\mathbf{v}}|_k)_{\mathbf{L}^2(0,T)} \tag{28}$$

and the functional $f_\mathcal{T} : \mathbf{H}_\mathcal{T} \to \mathbb{R}$

$$f_\mathcal{T}(\mathbf{v}) \coloneqq \sum_{k\in\mathcal{N}_F} (\mathbf{f}_k, \dot{\mathbf{v}}|_k)_{\mathbf{L}^2(0,T)}.$$

We define the energy of the truss system as sum of energies of all members

$$\mathcal{E}_\mathcal{T}(\mathbf{u},t) \coloneqq \sum_{m\in\mathcal{T}} \mathcal{E}(u_m,t) \geq 0.$$

The sum in (28) can be extended to all $k \in \mathcal{N}_\mathcal{T}$ since contributions of nodes in $\mathcal{N}_\mathcal{S}$ vanish for functions in $\mathbf{H}_\mathcal{T}$. By changing order of summation we obtain

$$\begin{aligned} a_\mathcal{T}(\mathbf{u},\mathbf{u}) &= \sum_{k\in\mathcal{N}_\mathcal{T}} \sum_{m\in\beta_k} (\mathbf{p}_m|_k, \dot{\mathbf{u}}_m|_k)_{\mathbf{L}^2(0,T)} = \sum_{m\in\mathcal{T}} \sum_{k\in\kappa_m} (\mathbf{p}_m|_k, \dot{\mathbf{u}}_m|_k)_{\mathbf{L}^2(0,T)} \\ &= \sum_{m\in\mathcal{T}} (p_m|_{\kappa_m}, \dot{u}_m|_{\kappa_m})_{L^2(0,T)\times L^2(0,T)} = \mathcal{E}_\mathcal{T}(\mathbf{u},T) \end{aligned}$$

for any $\mathbf{u} \in \mathbf{H}_\mathcal{T}$, which is the desired energy identity at final time. Assuming that

$$T \leq \min_{m\in\mathcal{T}} \frac{L_m}{c_m} \tag{29}$$

holds, we have $\mathrm{C}_m = \mathrm{I}$ for every $m \in \mathcal{T}$. Hence, the Dirichlet-to-Neumann map of each rod acts as scaled time derivative and we obtain for any $\mathbf{u} \in \mathbf{H}_\mathcal{T}$

$$\begin{aligned} \mathcal{E}_\mathcal{T}(\mathbf{u},T) &= \sum_{m\in\mathcal{T}} \tfrac{E_m A_m}{c_m} \|\dot{u}_m|_{\kappa_m}\|^2_{L^2(0,T)} = \sum_{k\in\mathcal{N}_F} \sum_{m\in\beta_k} \tfrac{E_m A_m}{c_m} \|\dot{\mathbf{u}}|_k \cdot \mathbf{r}_m\|^2_{L^2(0,T)} \\ &= \sum_{k\in\mathcal{N}_F} (J_k \dot{\mathbf{u}}|_k, \dot{\mathbf{u}}|_k)_{\mathbf{L}^2(0,T)} \gtrsim \sum_{k\in\mathcal{N}_F} \|\dot{\mathbf{u}}|_k\|^2_{\mathbf{L}^2(0,T)} = \|\dot{\mathbf{u}}\|^2_{\mathbf{L}^2(\Sigma_\mathcal{T})} \end{aligned}$$

where we used the positive definiteness of J_k for each $k \in \mathcal{N}_F$. We conclude that the energetic bilinear form (28) is elliptic if (29) holds. Similarly to Section 2.1 formulation (27) solves for the unknown displacement functions of all truss nodes in $[0,T]$ in one shot. In the following subsection we develop an equivalent approach that decomposes (27) into a set of simpler variational formulations posed on subintervals. This is an extension of the ideas of Section 2.2 from single rod problems to truss systems.

Remark 2. Our notation only accounts for mechanical supports that prevent the displacement of a node in any direction. However, Figure 3 indicates a support that prevents only vertical movement of node k_3. Although the notation cannot account for such conditions, our implementation is indeed capable of doing so. In order to account for such systems, the equilibrium condition (22) has to be considered only in the unsupported directions while the truss space (26) has to enforce zero displacements only in the supported directions. We resort to the simplified notation, since the essential concepts we wish to convey are fully covered by it, and an excess of technical intricacies is avoided.

3.2 Stepwise solution of truss problems

To come up with a stepwise approach for solving (27), we first study the action of the nodal force operator (24) in more detail. We restrict our attention to one observed node $k \in \mathcal{N}_F$ for now. For each member $m \in \beta_k$ we introduce $\chi_{m,k} := \kappa_m \setminus k$, which is the one node connected to member m that is not the observed node k. By careful inspection of (23) we find the explicit representation

$$\mathrm{P}_k \mathbf{u} = J_k \dot{\mathbf{u}}|_k + 2 \sum_{m \in \beta_k} M_m \sum_{j=1}^{n_m - 1} \mathrm{S}_m^{2j} \dot{\mathbf{u}}|_k - 2 \sum_{m \in \beta_k} M_m \sum_{j=0}^{n_m - 1} \mathrm{S}_m^{2j+1} \dot{\mathbf{u}}|_{\chi_{m,k}}. \tag{30}$$

Insertion of (30) into (25) leads us to the conclusion that a time local solution can be found easily, if the shift operators act only on parts of the solution that are already known. In that case only J_k acts on the yet unknown part of the solution. Thus, the main idea of this subsection is to decompose the solution $\mathbf{u} \in \mathbf{H}_{\mathcal{T}}$ similarly to Section 2.2, which enables a sequential solution approach. To achieve this, a suitable partitioning of the skeleton $\Sigma_{\mathcal{T}}$ into subdomains has to be found. Since each node may be connected to members of different length and propagation speed, the size of these segments has to be the shortest travel time of all attached members. Therefore, a decomposition of $\Sigma_{\mathcal{T}}$ into space-time slabs is not desirable, however, the time interval $[0,T]$ has to be subdivided independently for each truss node. Hence, the interval length

$$\Delta t_k := \min_{m \in \beta_k} \frac{L_m}{c_m}$$

and the number of time steps

$$n_k := \left\lceil \frac{T}{\Delta t_k} \right\rceil$$

are defined for each $k \in \mathcal{N}_{\mathcal{T}}$. Note that one could actually choose any Δt_k smaller than above definition and all of the following derivations would still be valid. Here, we use the largest interval length such that the short-time ellipticity discussed in Section 3.1 carries over to the local variational problems. By introducing the time steps

$$t_{k,j} := \begin{cases} j\Delta t_k & j = 0, \dots, n_k - 1, \\ T & j = n_k \end{cases}$$

an appropriate decomposition of the time interval $[0,T]$ is given by

$$\Upsilon_{k,j} \coloneqq \left[t_{k,j-1}, t_{k,j}\right], \quad j = 1, \ldots, n_k$$

for each $k \in \mathcal{N}_T$. Using this partitioning the extension of a nodal time local displacement function $\mathbf{u}_{k,j} : \Upsilon_{k,j} \to \mathbb{R}^d$ to $\widetilde{\mathbf{u}}_{k,j} : (0,T) \to \mathbb{R}^d$ is defined similarly to the single rod case

$$\widetilde{\mathbf{u}}_{k,j}(t) \coloneqq \begin{cases} \mathbf{u}_{k,j}(t) & t \in \Upsilon_{k,j}, \\ \mathbf{u}_{k,j}\left(t_{k,j}\right) & t \in \left(t_{k,j}, T\right], \\ \mathbf{0} & t \in \left[0, t_{k,j-1}\right). \end{cases}$$

Consequently, we obtain the decomposition of the displacement function

$$\mathbf{u}|_k(t) = \sum_{j=1}^{\ell} \widetilde{\mathbf{u}}_{k,j}(t), \quad t \in \bigcup_{j=1}^{\ell} \Upsilon_{k,j} \tag{31}$$

for each node k. The local components of the nodal solution $\mathbf{u}_{k,j}$ are computed by solving a time local variational formulation of the nodal equilibrium. This form is obtained by projecting (25) onto the time derivative of a suitable displacement test function defined on $\Upsilon_{k,j}$. In this context, representation (30) in conjunction with (31) is employed. The local problem at node $k \in \mathcal{N}_F$ for $j \in \{1, \ldots, n_k\}$ reads:
Find $\mathbf{u}_{k,j} \in \mathbf{H}^1_{\{0\}}\left(\Upsilon_{k,j}\right)$ such that

$$b_{\mathcal{T}}^{k,j}\left(\mathbf{u}_{k,j}, \mathbf{v}_j\right) = \left(\mathbf{f}_k, \dot{\mathbf{v}}_j\right)_{\mathbf{L}^2\left(\Upsilon_{k,j}\right)} - g_{\mathcal{T}}^{k,j}\left(\mathbf{v}_j\right) \tag{32}$$

holds for all $\mathbf{v}_j \in \mathbf{H}^1_{\{0\}}\left(\Upsilon_{k,j}\right)$. The bilinear form $b_{\mathcal{T}}^{k,j} : \mathbf{H}^1_{\{0\}}\left(\Upsilon_{k,j}\right) \times \mathbf{H}^1_{\{0\}}\left(\Upsilon_{k,j}\right) \to \mathbb{R}$ is defined by

$$b_{\mathcal{T}}^{k,j}\left(\mathbf{u}_{k,j}, \mathbf{v}_j\right) \coloneqq \left(J_k \dot{\mathbf{u}}_{k,j}, \dot{\mathbf{v}}_j\right)_{\mathbf{L}^2\left(\Upsilon_{k,j}\right)} \tag{33}$$

and the functional $g_{\mathcal{T}}^{k,j} : \mathbf{H}^1_{\{0\}}\left(\Upsilon_{k,j}\right) \to \mathbb{R}$ reads

$$g_{\mathcal{T}}^{k,j}\left(\mathbf{v}_j\right) \coloneqq 2 \sum_{m \in \beta_k} \sum_{\ell=1}^{n_m - 1} \left(M_m \, \mathrm{S}_m^{2\ell} \, \dot{\mathbf{u}}|_k, \dot{\mathbf{v}}_j\right)_{\mathbf{L}^2\left(\Upsilon_{k,j}\right)} - 2 \sum_{m \in \beta_k} \sum_{\ell=0}^{n_m - 1} \left(M_m \, \mathrm{S}_m^{2\ell+1} \, \dot{\mathbf{u}}|_{\chi_{m,k}}, \dot{\mathbf{v}}_j\right)_{\mathbf{L}^2\left(\Upsilon_{k,j}\right)} \tag{34}$$

which represents the interactions with the solution on previous time steps. Due to these interplays, above procedure has a sequential nature. In particular, the first term in (34) is determined by the past of the observed node k, while the second one results from the past of all adjacent nodes. Consequently, for a fixed $k \in \mathcal{N}_F$ one cannot just advance the local index j from 1 to n_k, since the required parts of the solution of the neighbouring nodes will be missing. In that case, one has to proceed to a different node in $\mathcal{N}_F$ where all interactions in (34) are known. Repetition of this procedure leads to a solution approach that is sequential in both the considered node $k \in \mathcal{N}_F$ as well as the considered time interval $j \in \{1, \ldots, n_k\}$. The positive definiteness

of J_k ensures ellipticity of the bilinear form (33), and consequently existence and uniqueness of the solution of (32). Furthermore, any conforming discretization of the variational problem is stable.

The reader might notice that our approach, especially in the stepwise representation (32)–(34), strongly resembles the method of Digital Waveguide Meshes, see e.g. [31, 23]. Within this procedure a discretization in space and time is introduced, facilitating a system of delay lines for each rod (or acoustic string in the case of the cited references). Using this discretization the method mimics the characteristics of the wave equation in a discrete sense. Moreover, certain coupling conditions at the hinges (or junctions) ensure the physical compatibility of the connected waveguide elements. As our approach based on retarded potentials always constructs exact solutions of the wave equation, one can also clearly observe its characteristics within the algorithm. The main difference is that the time domain BIE method does not need to discretize the rods but only the coupling junctions.

3.3 On the extension of the model

To account for transversal accelerations, transversal inner forces, and bending moments, the incorporation of dynamic Timoshenko beam theory seems viable. However, its time domain fundamental solution is substantially more involved when compared to the wave equation [25, Ex. 3.5.4 and 4.1.6]. To enable a formulation similar to the one proposed in this section, an operator that maps the kinematic quantities (transversal deflection and rotation at Σ) to the associated kinetic ones (bending moment and transversal force at Σ) is necessary. For the Timoshenko beam a relation comparable to (5) can indeed be derived. However, to the best of our knowledge, an exact representation of this map like (10) is not known. The simplest way to circumvent this issue, is to replace the exact map by an approximate one. This idea is explained in, e.g. [29, Ch. 12.3 and 12.4] for elliptic boundary value problems.

For contributions that consider time-domain BIEs of damped rods in one-dimensional space the reader is referred to [5, 3]. Again, it appears more practical to approximate the Dirichlet-to-Neumann map in this case rather than attempting to find an exact representation.

4 Space-time discretization

The first step in the discretization phase is to decompose the time interval $[0,T]$ into $N \in \mathbb{N}$ subintervals. To do so, consider $N+1$ time steps with $0 = t_0 < t_1 < t_2 < \cdots < t_{N-1} < t_N = T$. This gives rise to N elements $\tau_\ell := [t_{\ell-1}, t_\ell]$ for $\ell = 1, \ldots, N$. The union of elements is the line mesh $I_N := \bigcup_{\ell=1}^{N} \tau_\ell$. We particularly emphasize that these elements need not be uniform, i.e. $|\tau_\ell|$ does not need to equal $|\tau_m|$ for $\ell \neq m$. This condition is necessary for enabling adaptive mesh refinement as described below.

As observed in the previous sections an H^1-conforming finite element space is required to reach a proper Galerkin discretization of the variational problems. In this paper, only the basic finite element space of continuous piecewise linear functions

$$S^1(I_N) := \left\{ \varphi \in C(0,T) : \varphi|_\tau \in \mathbb{P}^1(\tau), \tau \in I_N \right\}$$

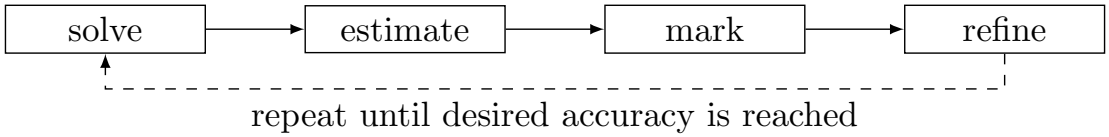

Figure 4: Depiction of the adaptive refinement strategy.

is considered. Since derivatives of functions in this space are piecewise constant, a remarkably efficient realization of the discussed bilinear forms is possible. Note that the integrals associated with external loading functions are approximated by standard Gauss-Legendre quadrature rules.

Transient solutions to problems of wave propagation may be especially difficult to approximate, and thus it is desirable to design a method that can adapt automatically and locally to the solution. A usual approach to adaptivity is to compute an error indicator measuring the quality of the approximation for each element of the current mesh. Based on these indicators, a set of elements is chosen (marked) for further refinement. Finally, the marked elements are refined, leading to a new mesh, on which the subsequent simulation is carried out. This process, which is repeated until a certain quality of approximation is reached, is depicted in Figure 4. In the following, the choice of a suitable error indicator is discussed for both the Robin problem and the truss problem. The employed strategies for marking and refining are addressed at the end of this section.

4.1 Discretization of Robin single rod problems

The two time intervals of Σ are decomposed independently, i.e. $\mathcal{G}_N := \{0\} \times I_{N_0} \cup \{L\} \times I_{N_L}$, where $N := N_0 + N_L$ is the number of elements at both end points. To obtain a conforming space, the initial condition has to be passed onto the finite element space, leading to the N-dimensional trial space $U_N := \left(S^1(I_{N_0}) \times S^1(I_{N_L})\right) \cap H^1_{\{0\}}(\Sigma)$. The discrete problem is to find $u_N \in U_N$ such that

$$a(u_N, v_N) + (K_s u_N, \dot{v}_N)_{L^2(\Sigma)} = (f, \dot{v}_N)_{L^2(\Sigma)}$$

holds for all $v_N \in U_N$. The discretization of the stepwise solution procedure (17) follows the same concept.

As mentioned previously, some measure that indicates the error for each element is needed to come up with an adaptive scheme. The chosen error indicator is based on the following observation. Due to the conformity of the trial space, any $u_N \in U_N$ satisfies (1) and (2) for any chosen mesh. The only condition which (in general) is not satisfied exactly is the boundary condition (3). Thus, it seems natural to measure the quality of an approximation by considering the residual of this very equality. Consequently, we define the error indicator

$$\eta_\tau := \|\mathrm{DtN}\, u_N + K_s u_N - f\|_{L^2(\tau)}$$

for each element $\tau \in \mathcal{G}_N$. Note that the same error indicator is used for the sequential solution approach by space-time slabs. In this case, the indicators are computed only on the slab currently

under consideration. Furthermore, the function u_N is split up as in (16).

4.2 Discretization of truss problems

The time interval is decomposed separately for each truss node. Hence, we consider meshes I_{N_k}, where N_k is the number of elements at node k, and define the total number of elements $N \coloneqq \sum_{k\in\mathcal{N}_T} N_k$. A Galerkin discretization of (27) is achieved by restriction to the finite-dimensional trial space $\mathbf{U}_N \coloneqq \left(\bigtimes_{k\in\mathcal{N}_T} \mathbf{S}^1\left(I_{N_k}\right)\right) \cap \mathbf{H}_T$. The discrete problem is to find $\mathbf{u}_N \in \mathbf{U}_N$ such that

$$a_T\left(\mathbf{u}_N, \mathbf{v}_N\right) = f_T\left(\mathbf{v}_N\right)$$

holds for all $\mathbf{v}_N \in \mathbf{U}_N$. By construction, the only approximation error occurs in the nodal equilibrium equation (22). Thus, the chosen error indicator

$$\eta_\tau \coloneqq \left\| \mathrm{P}_k \mathbf{u}_N - \mathbf{f}_k \right\|_{\mathbf{L}^2(\tau)}$$

for each element $\tau \in I_{N_k}$ and each $k \in \mathcal{N}_F$ seems to suggest itself. Again, the stepwise solution approach (32) is treated in the same fashion, i.e. above techniques are just applied to the currently observed time step.

At this point, it is worth mentioning that a uniform decomposition of the time interval could significantly reduce the computational costs. If the time steps were uniform for every truss node the interaction matrices realizing (34) could be precomputed once for every member. In particular, it would be sufficient to compute the discrete versions of S_m^k for $k = 0, \ldots, n_m$ tested only at the last element. The operators tested on previous elements could be obtained by truncating the sum and shifting the indices of the involved elements. This approach has the great advantage of reducing the original quadratic complexity $O(T^2)$ of the algorithm to a mere linear one $O(T)$ in the simulation end time. However, we lay a focus on a method capable of capturing local features and non-smooth solutions with high accuracy. That is why we do not use the simplification of a uniform mesh and choose to work with arbitrary decompositions of the time interval instead. It shall be noted that in both cases the algorithm has linear complexity in the discretization parameter $O(N)$. This is due to the fact that for each element there is a maximum number of nonzero shifts that is independent of N.

4.3 Adaptive mesh refinement

Once the error indicators η_τ are computed for each element τ, the next step is to mark a set of elements based on these indicators. There are many different strategies for element marking. We restrict our considerations to a straightforward approach, which yields promising results. This scheme was introduced by Dörfler [14] and is often referred to as *Dörfler marking*. Within this procedure, the set of marked elements $\mathcal{M} \subseteq \mathcal{G}_N$ is the smallest set such that

$$\sum_{\tau\in\mathcal{M}} \eta_\tau^2 \geq \gamma \sum_{\tau\in\mathcal{G}_N} \eta_\tau^2$$

holds with some $\gamma \in (0,1)$.

The final ingredient of an adaptive procedure is the actual refinement strategy for marked elements. In our case of line segments we resort to the simplest approach of dividing each marked element into two subintervals of equal size.

5 Numerical examples

In this section, we present numerical examples verifying the implementation and the adaptive mesh refinement of the proposed method for a single rod. To test the implementation for truss systems, we shall experimentally investigate the convergence of a set of solutions obtained by the adaptive strategy towards a high-resolution reference solution. In the final example, a typical truss girder of a small bridge is examined.

The arising sparse linear systems of equations are solved by the *MATLAB* backslash operator [22].

5.1 Numerical examples for the Robin problem

We consider a rod of unit length and unit material parameters. Moreover, we set $T = 6$, and thus the number of summands in the operator C of the Dirichlet-to-Neumann map is $n = 3$. Hence, this configuration helps confirm the correctness of the explicit representation of this operator.

I. Convergence study. To confirm the convergence of the proposed methods we first investigate a problem with a sufficiently smooth solution. To this extent, we consider the solution

$$u(x,t) = \frac{1}{100}\left(t - \left|x - \tfrac{3}{2}\right|\right)^3 \theta\left(t - \left|x - \tfrac{3}{2}\right|\right), \quad (x,t) \in \mathbb{R}^2$$

which is illustrated in Figure 5a. Furthermore, the non-smooth solution

$$u(x,t) = \left|\sin\left(t - \left|x - \tfrac{4}{3}\right|\right)\right| \theta\left(t - \left|x - \tfrac{4}{3}\right|\right), \quad (x,t) \in \mathbb{R}^2$$

is intended to support the discussed error indicator and the strategy for adaptive mesh refinement. This function is depicted in Figure 5b. The corresponding Robin data of these solutions are computed via (3) and provided as right hand side for the approximation. The forcing functions inducing the smooth solution are

$$f_0(t) = \frac{3}{100}\left[-\left(t - \tfrac{3}{2}\right)^2 + \left(t - \tfrac{3}{2}\right)^3\right] \theta\left(t - \tfrac{3}{2}\right),$$
$$f_1(t) = \frac{3}{100}\left[\left(t - \tfrac{1}{2}\right)^2 + \left(t - \tfrac{1}{2}\right)^3\right] \theta\left(t - \tfrac{1}{2}\right),$$

which are provided here to make the concept of manufactured solution more comprehensible.

In the following three procedures are examined. The solution is approximated by both the one-shot and the stepwise solution approaches using uniform mesh refinement. Additionally, the solution is approximated by the one-shot approach employing adaptive mesh refinement with $\gamma = 0.4$. The error is measured in the energy norm $\|\dot{u} - \dot{u}_N\|_{L^2(\Sigma)}$ and compared to the discretization parameter N.

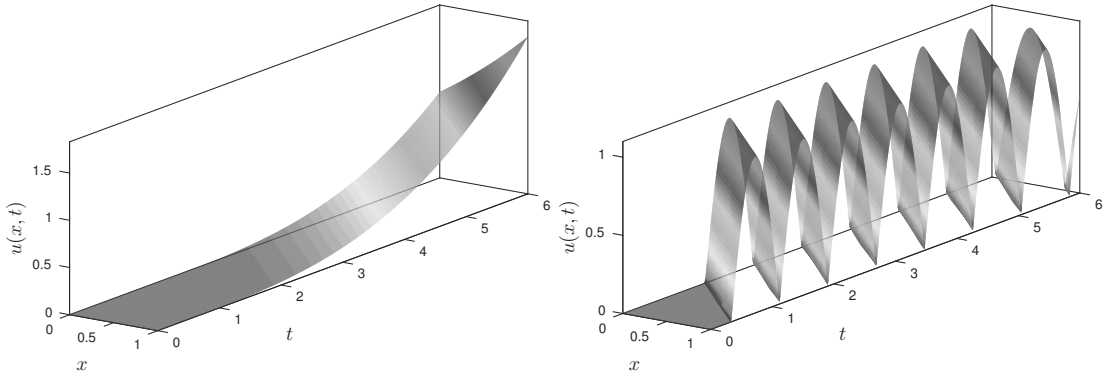

(a) Smooth solution. (b) Non-smooth solution.

Figure 5: **I. Convergence study.** Illustrations of the employed d'Alembert solutions.

In Figure 6a, the results are depicted for the smooth solution. It can be observed that all examined methods reach the optimal linear convergence rate in the energy norm well-known for the employed space of hat functions. In particular, the one-shot and the stepwise approach compute the same approximation on the same grid, thus their respective errors coincide.

The situation changes when the non-smooth solution is considered, see Figure 6b. The observed rates of convergence for uniform mesh refinement break down to $1/2$, due to the low regularity of the solution. Again, both methods yield the same approximations and errors, underlining their equivalence in the case of non-adaptive mesh refinement. Moreover, it can be observed that the employed strategy for adaptive mesh refinement is indeed capable of restoring the optimal linear convergence in the number of unknowns for the examined solution.

Figure 7 provides an illustration of the behaviour of the adaptive mesh refinement. The solution is approximated by the stepwise approach using the discussed error indicator. Each slab is initially discretized by two elements per side and refined using $\gamma = 0.4$ and ten steps of refinement. It can be observed that in those slabs with two kinks in the solution, e.g. at $x = L$ and $t \in [1,2]$, the refinement is highly concentrated at these two points. In the other slabs the refinement also focuses on the apex of the function, since the second derivative takes its largest value at this location.

We wish to emphasize that the presented results are quite similar to results provided in the literature. In [32], the Dirichlet problem of the 1D wave equation is discretized by the energetic BEM. An error indicator based on Calderón identities is proposed and its performance is investigated by means of numerical experiments. These examples are analogous to those displayed in this section, and their obtained results feature a high degree of similarity to our findings. Hence, for the examined solutions our proposed error indicator for the Robin problem performs quite similar to more complicated error estimators based on deeper knowledge of the BIE formulation.

II. Impact load. A frequently used benchmark for linear elastodynamics is a rod excited by impact load, see e.g. [18, 30, 28]. Unlike the cited references, we do not consider a bar which is fixed at one end. However, the examined solution depicted in Figure 8 has a similar shape and poses the same difficulties in terms of approximation. Again, this function is used

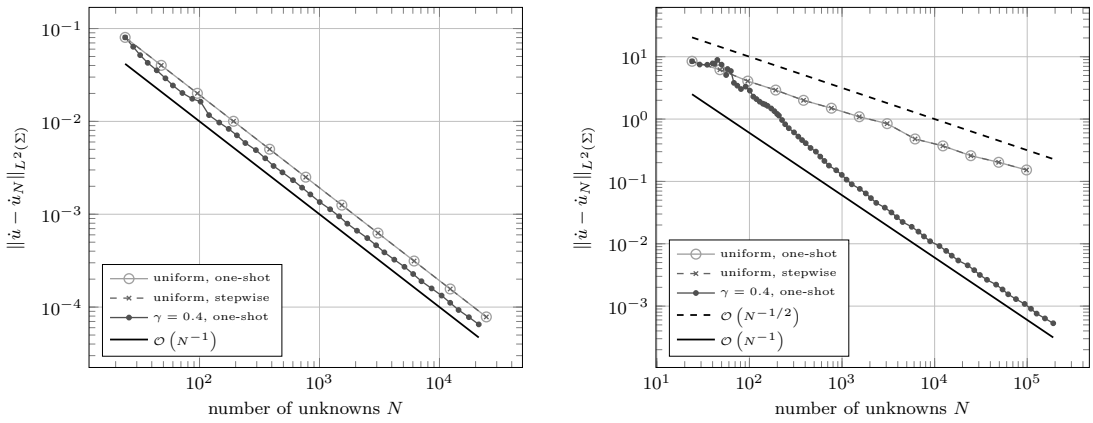

(a) Errors of the smooth solution.

(b) Errors of the non-smooth solution.

Figure 6: **I. Convergence study.** Error plots for the Robin single rod problem.

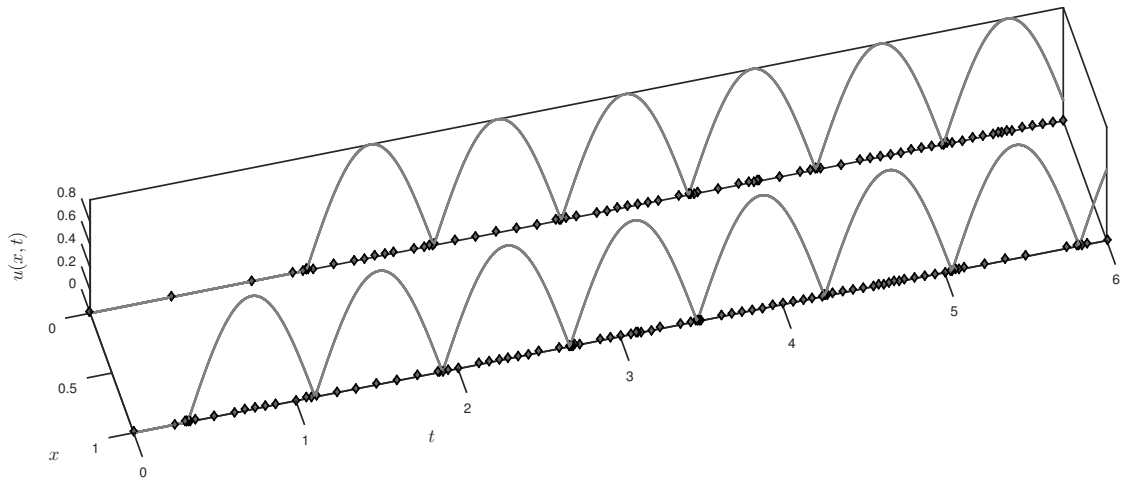

Figure 7: **I. Convergence study.** Adaptively refined mesh obtained by ten steps of refinement per slab with $\gamma = 0.4$. The markers indicate the time steps.

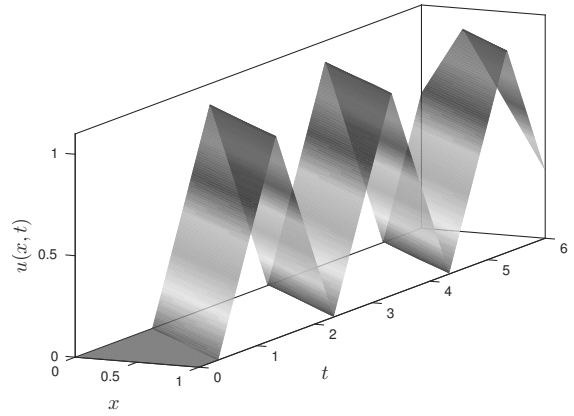

Figure 8: **II. Impact load.** Typical solution arising for impact loads.

as a manufactured solution. The approximations are computed by the stepwise approach and two examples are examined. In the first scenario, the kinks of the solution are aligned with the borders of the space-time slabs, while in the second case they are not aligned.

In Figure 9a, the results of the aligned mesh are provided. Each slab is discretized by two elements and the exact solution is obtained (apart form errors due to finite precision arithmetic). Hence, by application of the Dirichlet-to-Neumann map, we are able to recover the exact Neumann data as illustrated in Figure 9c. This feature is lost if the time steps do not align with the kinks of the solution as shown in Figure 9b. Five steps of adaptive refinement with $\gamma = 0.1$ are performed to show that the chosen error indicator can indeed improve the quality of the numerical solution by steering refinement towards its kinks. As a result, a reasonable approximation of the solution can be achieved using very few elements. It shall be especially noted that the approximate Neumann data $p_N = \mathrm{DtN}\, u_N$ displayed in Figure 9d are still an excellent approximation in this case. We emphasize that there are no overshoots in the approximation of the axial force, which are typically encountered within many classical methods, see e.g. [28]. Conventional approaches have to employ sophisticated finite element technology to approximate the discontinuities of the force function in space and time properly. In contrast, the mapping properties of the retarded layer potentials and the Dirichlet-to-Neumann map deal with this space-time discontinuity naturally. Hence, traditional discretization techniques can be employed for the arising BIEs and still convincing accuracy is achieved for such pulse-type loading scenarios.

5.2 Numerical examples for the truss problem

III. Tripod. As first model truss system we consider a three-dimensional tripod structure as depicted in Figure 10. The coordinates of the truss nodes with respect to the canonical basis $\{\mathbf{e}_1, \mathbf{e}_2, \mathbf{e}_3\}$ in $\mathbb{R}^3$ are

$$x_{k_1} = (0,0,0)^\top,\ x_{k_2} = (3,0,0)^\top,\ x_{k_3} = (0,3,0)^\top,\ x_{k_4} = (1,2,3)^\top.$$

The material parameters of all members are set to unit values. At the top node, which is the only free node, the pulse loading

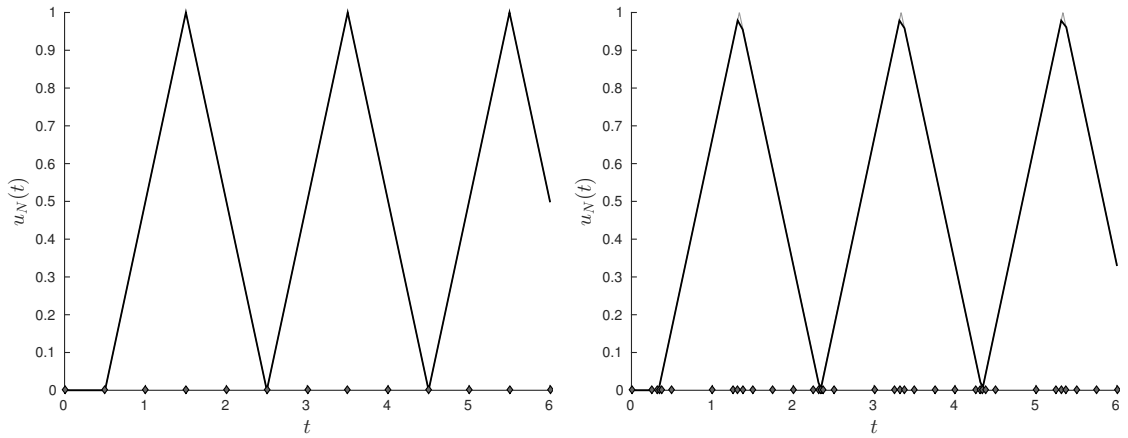

(a) Aligned mesh, $u_N \equiv u$.

(b) Non-aligned refined mesh, $u_N \approx u$.

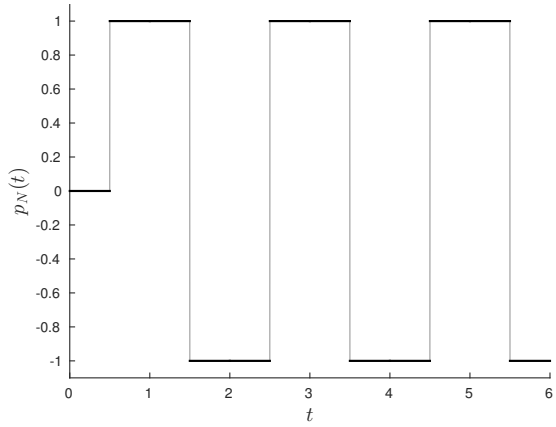

(c) Aligned mesh, $p_N \equiv p$.

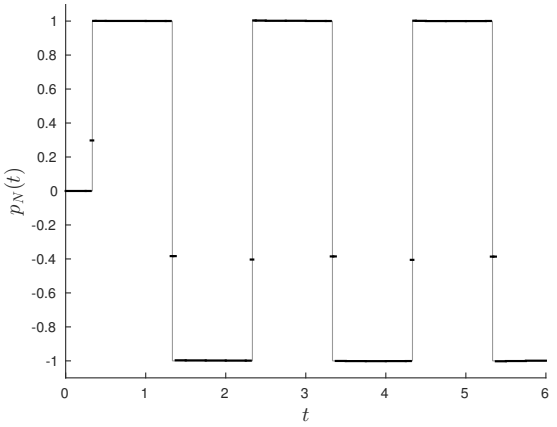

(d) Non-aligned refined mesh, $p_N \approx p$.

Figure 9: **II. Impact load.** Cauchy data at $x = L$ for the solution due to impact load. The light grey lines indicate the exact solution. The first row shows the Dirichlet data u_N and below the corresponding Neumann data p_N are displayed. The time steps are represented by the markers.

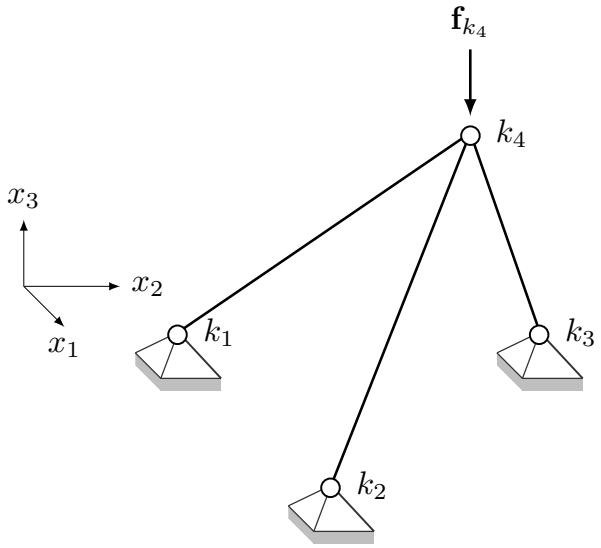

Figure 10: **III. Tripod.** Sketch of the considered tripod system.

$$\mathbf{f}_{k_4}(t) \coloneqq -\frac{1}{20}\left[\theta(t) - \theta(t-1)\right]\mathbf{e}_3$$

is applied. The simulation end time is fixed to $T = 30$ and the one-shot solution strategy is employed for solving this problem. In the following we examine the displacement of the free node k_4.

First, we consider a mesh with $N = 5000$ time steps of uniform size. The result is shown in Figure 11 and one can see that the sharp features of the components of the displacement vector $\mathbf{u}|_{k_4}$ are resolved quite accurately. This approximation shall act as reference solution for the following considerations. To confirm the proposed error indicator, we simulate the same problem using an initial mesh with $N = 10$ uniform time steps and employ 120 steps of adaptive refinement with $\gamma = 0.05$. Since γ is chosen quite small, we expect that the adaptive refinement will be focused towards the critical points. The obtained solution and the refined mesh, which has $N = 129$ elements, are depicted in Figure 12a. Indeed refinement concentrates on the kinks of the displacement function, similar to the single rod case studied previously. To put this result into perspective, Figure 12b illustrates the approximation obtained by a uniform mesh with $N = 150$ elements. One can observe that the kinks of the solution are not resolved in the desired fashion. To get a quantitative comparison of these two approximations, we compute their distance to the reference solution. The relative distance in the energy norm is defined

$$d_N(t_i) \coloneqq \frac{\|\dot{\mathbf{u}}_{5000}|_{k_4} - \dot{\mathbf{u}}_N|_{k_4}\|^2_{\mathbf{L}^2(t_{i-1},t_i)}}{\|\dot{\mathbf{u}}_{5000}|_{k_4}\|^2_{\mathbf{L}^2(0,T)}}, \quad i = 1,\ldots,5000 \tag{35}$$

where the time steps t_i are taken from the mesh of the reference solution. Moreover, the function $d_N : [0,T] \to \mathbb{R}$ is defined as linear interpolation of (35) to provide better readability. The regions where the values of d_N are large represent locations where the approximation is poor. The result

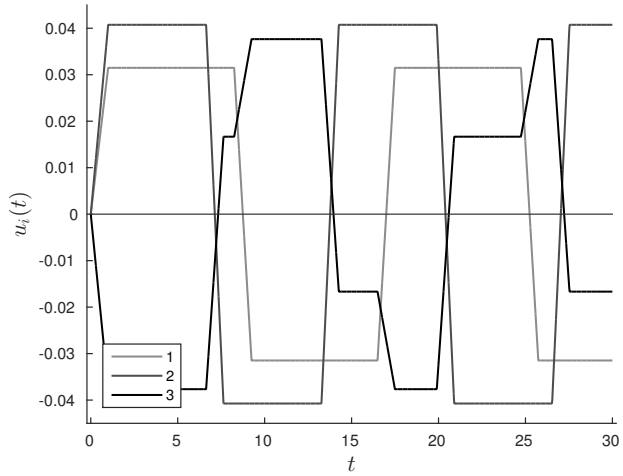

Figure 11: **III. Tripod.** Reference solution, displacement of free node $\mathbf{u}_{5000}|_{k_4}$. The indices $1,2,3$ represent the component of the displacement vector.

for the adaptively refined mesh is shown in Figure 12c, whereas the coarse uniform mesh is depicted in Figure 12d. We observe that the distance of the adaptively steered solution is on the one hand substantially smaller and on the other hand its peaks are significantly narrower. The relative distance of the solution on the uniform mesh is roughly 6.2% while the adaptively refined solution enjoys a relative distance of only 1.6%. Although the latter is obtained by fewer elements, its distance is nearly four times smaller.

From an engineering point of view, interior forces play an important role in the design of structures. Consequently, we should also compare the axial forces obtained by the three considered approximations. In the following, we examine the longitudinal force in the middle of rod m_3, which connects nodes k_3 and k_4. The results are exhibited in Figure 13. One can clearly see that even the reference solution, depicted in Figure 13a is not flawless, however, it is still a reasonable approximation. On the one hand, Figure 13c illustrates that the coarse uniform mesh produces an rather crude force function that gets significantly worse as time progresses. On the other hand, the adaptively refined solution shown in Figure 13b has, at least from a visual inspection, the same quality as the reference. Furthermore, this result demonstrates that the overshoots observed on the uniform mesh can be removed by careful refinement.

All in all, these findings strongly advocate the use of adaptive mesh refinement for simulating wave phenomena in elastic truss structures, especially in the context of pulse-type loading scenarios. Moreover, the proposed error indicator performs reasonably well in the examined situations.

IV. Bridge. In the final example, we direct our attention towards a traditional problem encountered in structural engineering. We consider a short bridge, whose main girder is illustrated in Figure 14. It shall serve as typical example for steel railway bridges. All members are equipped with the same material parameters usual for structural steel

$$E = 200 \times 10^9\,\mathrm{Pa}, \quad \rho = 7850\,\mathrm{kg\,m^{-3}}, \quad A = 0.01\,\mathrm{m}^2$$

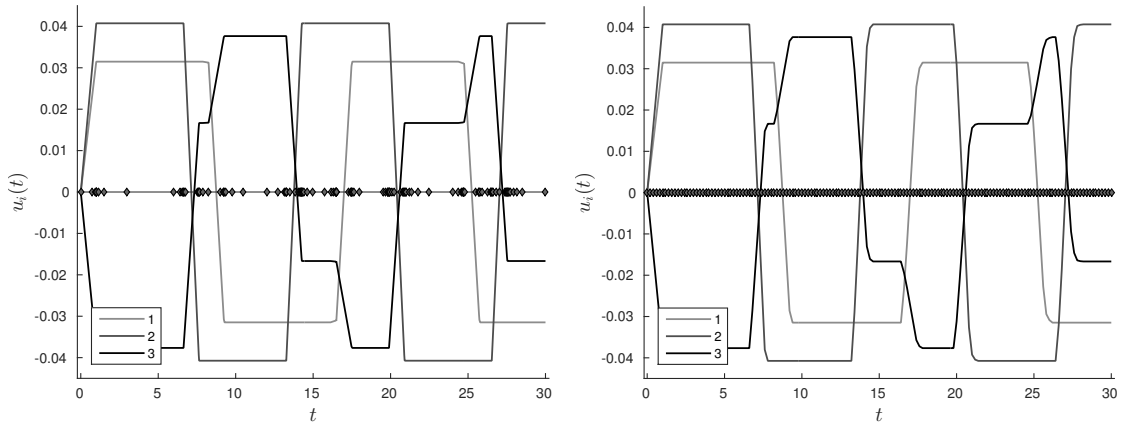

(a) Adaptively refined mesh, $N = 129$.

(b) Coarse uniform mesh, $N = 150$.

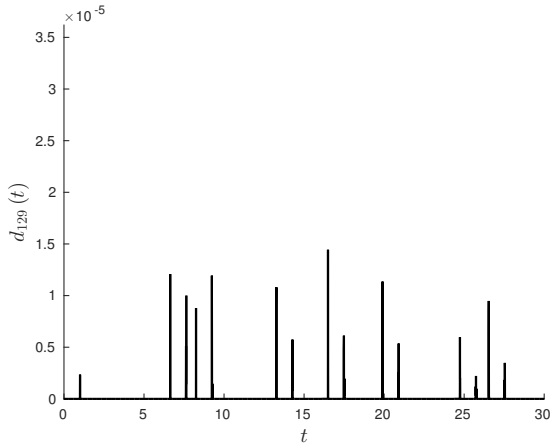

(c) Squared distance, $N = 129$.

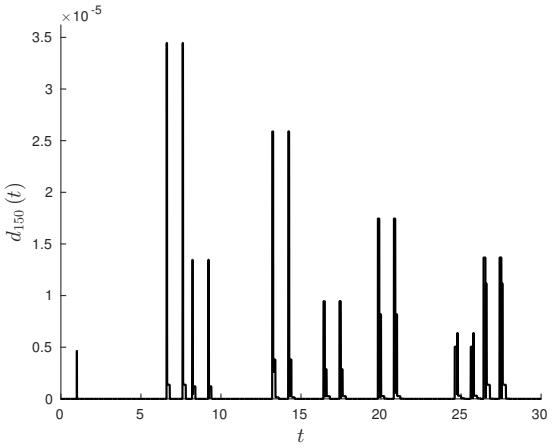

(d) Squared distance, $N = 150$.

Figure 12: **III. Tripod.** Displacement of free node $\mathbf{u}_N|_{k_4}$. The markers in the plots of the first row indicate the time steps. The second row shows the relative distance to the reference solution as a function in time.

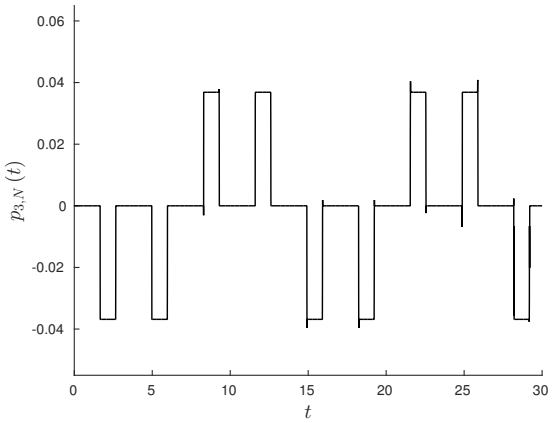

(a) Reference solution, $N = 5000$.

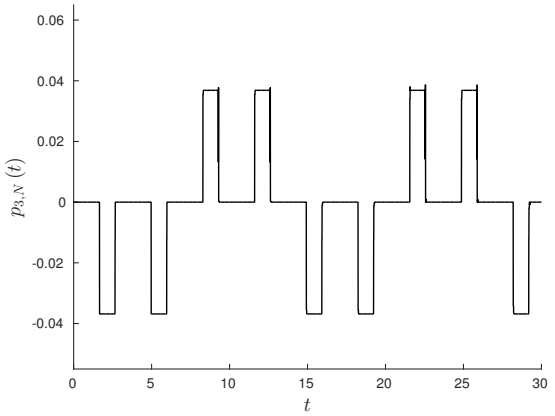

(b) Adaptively refined mesh, $N = 129$.

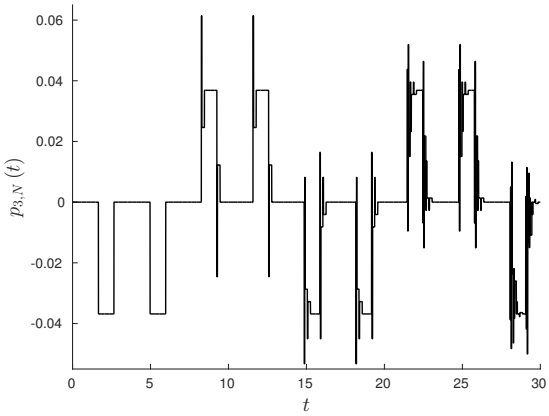

(c) Coarse uniform mesh, $N = 150$.

Figure 13: **III. Tripod.** Axial force function in the middle of of member m_3.

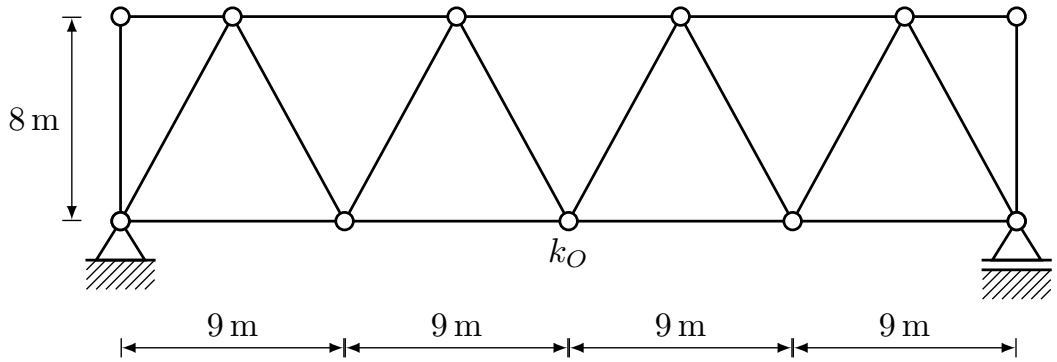

Figure 14: **IV. Bridge.** Sketch of the main girder of the railway bridge. The vertical displacement of the central node k_O is examined in Figure 17.

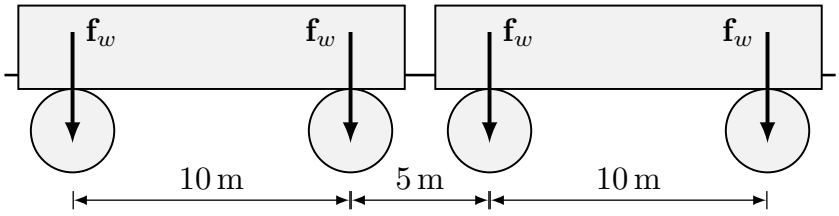

Figure 15: **IV. Bridge.** Configuration of the model train.

and consequently the wave velocity in each member is $c \approx 5047.5\,\mathrm{m\,s^{-1}}$. Our goal is to simulate the crossing of a small freight train. The configuration of the considered model train is depicted in Figure 15. Each wagon is assumed to have a mass of $m_w = 20 \times 10^3\,\mathrm{kg}$. Hence, the force at each wheel which is defined by

$$\mathbf{f}_w := -\frac{m_w g}{4}\mathbf{e}_2$$

has a magnitude of $50 \times 10^3\,\mathrm{N}$, where we used the gravitational acceleration $g = 10\,\mathrm{m\,s^{-2}}$ common in structural engineering. The train moves at a constant velocity of $25\,\mathrm{m\,s^{-1}}$. The rails are founded on a deck which is assumed to be rigid, such that the load of each wheel is distributed linearly by distance to the (at most) two neighbouring truss nodes.

In the considered simulation, we fix $T = 3\,\mathrm{s}$ and limit the train to three wagons. Due to this choice, the rear axis of the last wagon leaves the truss shortly after the simulation ends and a complete passage of the train is observed. We employ the stepwise solution approach with two elements per time slab. This discretization is refined by five iterations of adaptive refinement with $\gamma = 0.05$ for each time slab.

Figure 16 depicts the deformed truss structure at three distinct points in time. Apart from the obvious vertical displacement of the truss nodes, the horizontal movement of the rightmost node is clearly visible. Furthermore, Figure 17 exhibits the vertical displacement of the central node k_O. The peak amplitude is roughly 0.8 mm, which is a reasonable value for the examined case. One can observe that the displacement increases steadily as the train enters the bridge, while there is a state of almost harmonic oscillation afterwards. Finally, the displacement goes back to zero as the train leaves the structure. However, there exists no mechanism of damping in this system. Consequently, waves propagate at constant amplitude throughout the members, facilitating the build-up of oscillations as time progresses. We conclude that these results obtained by our approach based on retarded potentials are plausible and exceptionally competitive with data acquired by most classical time domain simulation methods.

6 Conclusion

We propose a new method for simulating elastodynamic truss structures by means of time domain boundary integral equations. In the employed mechanical model, transversal forces are neglected. Under this assumption a clear-cut framework, based on explicit knowledge of the dynamic Dirichlet-to-Neumann map, is established. The space-time formulation is built on con-

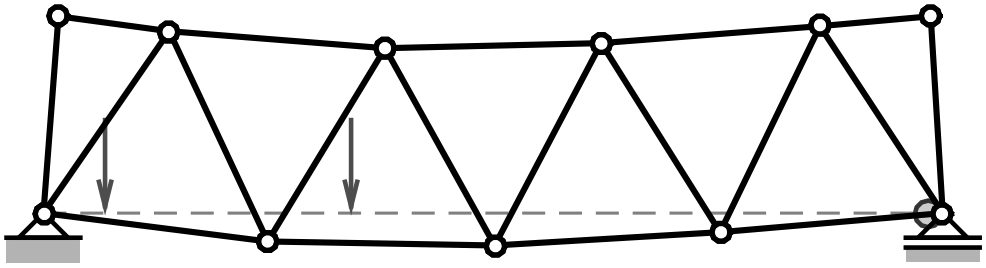

(a) Deformed configuration at $t = 0.5\,\mathrm{s}$.

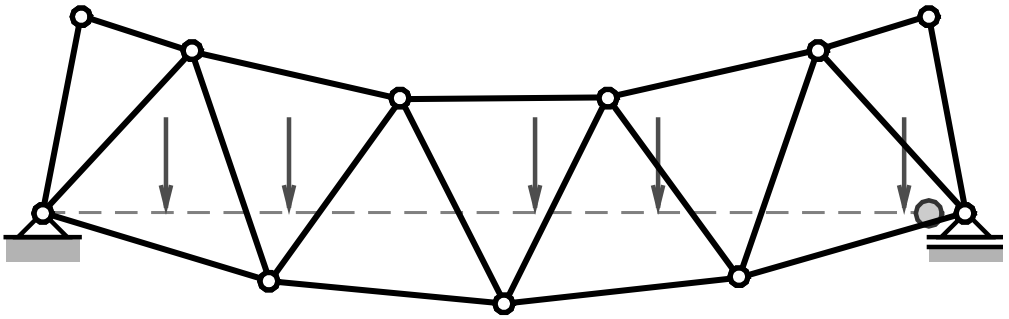

(b) Deformed configuration at $t = 1.4\,\mathrm{s}$.

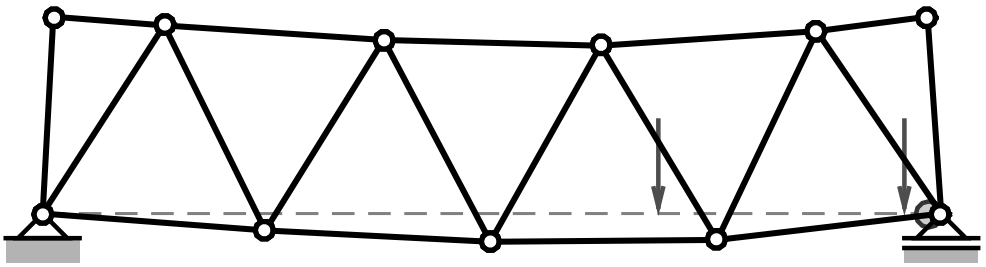

(c) Deformed configuration at $t = 2.6\,\mathrm{s}$.

Figure 16: **IV. Bridge.** Illustrations of deformed configurations (exaggerated) of the truss bridge. The position of the train is indicated by the force vectors of the wheels. The initial position of the right supported node is located at the grey disc.

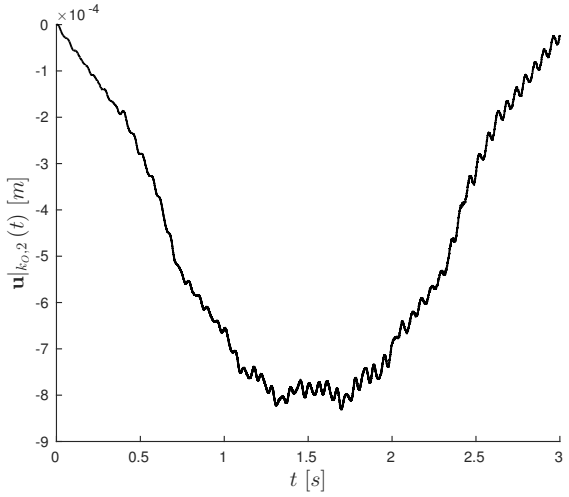

Figure 17: **IV. Bridge.** Vertical displacement of the central node k_O.

siderations related to the energy of the mechanical system. Moreover, a stepwise solution procedure is presented, which guarantees stable discretizations by exploiting the short-time ellipticity of the energy expression.

Numerical examples support the viability of the discussed procedures. Especially when dealing with solutions due to impact loads, the proposed formulations possess inherent advantages over many existing approaches. Furthermore, we provide an uncomplicated error indicator which enables adaptive mesh refinement and accurate resolution of local features.

By striving for an accessible formulation, we sacrificed generality in terms of the mechanical behaviour of the truss structure. At this point, the incorporation of transversal forces and inertia effects by means of Timoshenko beam theory is the missing component in developing a mechanically consistent framework for simulating elastodynamic truss systems. From an applied engineering point of view, integrating more complicated material behaviour, e.g. damping, seems desirable as well. Nevertheless, this work demonstrates that time domain boundary integral equations are a potent approach to simulating elastodynamic truss structures, with great advantages in many challenging loading scenarios.

References

[1] ABBOUD, T., JOLY, P., RODRÍGUEZ, J., AND TERRASSE, I. Coupling discontinuous Galerkin methods and retarded potentials for transient wave propagation on unbounded domains. *J. Comput. Phys. 230*, 15 (2011), 5877–5907.

[2] AIMI, A., AND DILIGENTI, M. A new space-time energetic formulation for wave propagation analysis in layered media by BEMs. *Int. J. Numer. Methods. Engrg. 75*, 9 (2008), 1102–1132.

[3] AIMI, A., DILIGENTI, M., AND GUARDASONI, C. Energetic BEM-FEM coupling for the numerical solution of the damped wave equation. *Adv. Comput. Math. 43*, 3 (2017), 627–651.

[4] AIMI, A., DILIGENTI, M., GUARDASONI, C., MAZZIERI, I., AND PANIZZI, S. An energy approach to space-time Galerkin BEM for wave propagation problems. *Int. J. Numer. Methods. Engrg. 80*, 9 (2009), 1196–1240.

[5] AIMI, A., DILIGENTI, M., GUARDASONI, C., AND PANIZZI, S. Numerical analysis of the damped wave equation by "Energetic" weak formulations. In *11th World Congress on Computational Mechanics, WCCM 2014, 5th European Conference on Computational Mechanics, ECCM 2014 and 6th European Conference on Computational Fluid Dynamics, ECFD 2014* (2014), pp. 3815–3826.

[6] AIMI, A., DILIGENTI, M., AND PANIZZI, S. Energetic Galerkin BEM for wave propagation Neumann exterior problems. *CMES Comput. Model. Eng. Sci. 58*, 2 (2010), 185–219.

[7] ANDERSON, M., AND KIMN, J.-H. A numerical approach to space-time finite elements for the wave equation. *J. Comput. Phys. 226*, 1 (2007), 466–476.

[8] ANTES, H., SCHANZ, M., AND ALVERMANN, S. Dynamic analyses of plane frames by integral equations for bars and Timoshenko beams. *J. Sound Vibration 276*, 3 (2004), 807–836.

[9] BAMBERGER, A., AND HA-DUONG, T. Formulation variationnelle espace-temps pour le calcul par potentiel retaré de la diffraction d'une onde acoustique (I). *Math. Meth. Appl. Sci. 8*, 3 (1986), 405–435.

[10] BAMBERGER, A., AND HA DUONG, T. Formulation variationnelle pour le calcul de la diffraction d'une onde acoustique par une surface rigide. *Math. Meth. Appl. Sci. 8*, 4 (1986), 598–608.

[11] CARRER, J., FLEISCHFRESSER, S., GARCIA, L., AND MANSUR, W. Dynamic analysis of Timoshenko beams by the boundary element method. *Eng. Anal. Bound. Elem. 37*, 12 (2013), 1602–1616.

[12] CHOPRA, A. K. *Dynamics of structures: theory and applications to earthquake engineering*, vol. 3. Prentice Hall New Jersey, 1995.

[13] COSTABEL, M. Time-dependent problems with the boundary integral equation method. In *Encyclopedia of Computational Mechanics*, E. Stein, R. de Borst, and T. J. R. Hughes, Eds., vol. 1, Fundamentals. John Wiley & Sons, New York, Chichester, Weinheim, 2005, ch. 25, pp. 703–721.

[14] DÖRFLER, W. A convergent adaptive algorithm for Poisson's equation. *SIAM J. Numer. Anal. 33*, 3 (1996), 1106–1124.

[15] GOPALAKRISHNAN, J., SCHÖBERL, J., AND WINTERSTEIGER, C. Mapped tent pitching schemes for hyperbolic systems. *SIAM J. Sci. Comput. 39*, 6 (2017), 1043-1063.

[16] HA-DUONG, T. On retarded potential boundary integral equations and their discretisation. In *Topics in Computational Wave Propagation*, M. Ainsworth, P. Davies, D. Duncan, B. Rynne, and P. Martin, Eds., vol. 31 of *Lecture Notes in Computational Science and Engineering*. Springer, 2003, ch. 8, pp. 301–336.

[17] HA-DUONG, T., LUDWIG, B., AND TERRASSE, I. A Galerkin BEM for transient acoustic scattering by an absorbing obstacle. *Int. J. Numer. Methods. Engrg. 57*, 13 (2003), 1845–1882.

[18] HAM, S., AND BATHE, K.-J. A finite element method enriched for wave propagation problems. *Comput. & Structures 94* (2012), 1–12.

[19] HULBERT, G., AND HUGHES, T. Space-time finite element methods for second-order hyperbolic equations. *Comput. Methods Appl. Mech. Engrg. 84*, 3 (1990), 327–348.

[20] LI, C., AND CHOU, T.-W. A structural mechanics approach for the analysis of carbon nanotubes. *Int. J. Solids Struct. 40*, 10 (2003), 2487–2499.

[21] LOWRIE, R. B., ROE, P. L., AND VAN LEERT, B. A space-time discontinuous Galerkin method for the time-accurate numerical solution of hyperbolic conservation laws. In *12th Computational Fluid Dynamics Conference* (1995), 135-150.

[22] MATLAB AND STATISTICS TOOLBOX. *Release R2015a*. The MathWorks Inc., Natick, Massachusetts, 2015.

[23] MURPHY, D., KELLONIEMI, A., MULLEN, J., AND SHELLEY, S. Acoustic modeling using the digital waveguide mesh. *IEEE Signal Process Mag. 24*, 2 (2007), 55–66.

[24] ODEGARD, G. M., GATES, T. S., NICHOLSON, L. M., AND WISE, K. E. Equivalent-continuum modeling of nano-structured materials. *Composites Science and Technology 62*, 14 (2002), 1869–1880.

[25] ORTNER, N., AND WAGNER, P. *Fundamental solutions of linear partial differential operators: Theory and practice*. Springer, 2015.

[26] RICHTER, G. R. An explicit finite element method for the wave equation. *Appl. Num. Math. 16*, 1-2 (1994), 65–80.

[27] SAYAS, F.-J. *Retarded Potentials and Time Domain Boundary Integral Equations: A Road Map*. Springer, 2016.

[28] SHANG, H., MACHADO, R., AND ABDALLA FILHO, J. Dynamic analysis of Euler–Bernoulli beam problems using the Generalized Finite Element Method. *Comput. & Structures 173* (2016), 109–122.

[29] STEINBACH, O. *Numerical approximation methods for elliptic boundary value problems: finite and boundary elements*. Springer Science & Business Media, 2007.

[30] TORII, A. J., AND MACHADO, R. D. Structural dynamic analysis for time response of bars and trusses using the generalized finite element method. *Lat. Am. J. Solids Struct. 9*, 3 (2012), 1–31.

[31] VAN DUYNE, S. A., AND SMITH, J. O. Physical modeling with the 2-D digital waveguide mesh. In *Proc. Int. Computer Music Conf.* (1993), pp. 40–47.

[32] ZANK, M., AND STEINBACH, O. Adaptive space-time boundary element methods for the wave equation. *Proc. Appl. Math. Mech. 16*, 1 (2016), 777–778.